



# Refraction and reflection patterns of an inclined turbulent conductive jet induced by a local transverse magnetic field

Alexander Vakhrushev<sup>a</sup>, Ebrahim Karimi-Sibaki<sup>a,b</sup>, Menghuai Wu<sup>b</sup>,  
Abdellah Kharicha<sup>a,b,\*</sup>

<sup>a</sup> Christian-Doppler Laboratory for Metallurgical Applications of Magnetohydrodynamics, Montanuniversität Leoben, Franz-Josef-Str. 18, A-8700 Leoben, Austria

<sup>b</sup> Chair of Simulation and Modeling of Metallurgical Processes, Montanuniversität Leoben, Franz-Josef-Str. 18, A-8700 Leoben, Austria

## ARTICLE INFO

### Keywords:

Magnetohydrodynamic jet  
Local magnetic field  
Refraction  
Expansion  
Relativistic jet bending  
Active galaxy nuclei

## ABSTRACT

This study investigates the interaction between turbulent conductive jets and transverse magnetic fields, focusing on the effects of jet inclination angle and magnetic field strength. This phenomenon is relevant to both metallurgy and astrophysics. In metallurgy, complex localized magnetic fields are frequently used to control molten metal flows. Similarly, in astrophysics, a comparable effect occurs with relativistic jets (RJs) emitted by active galactic nuclei (AGN), where these jets can be deflected or refracted when encountering magnetic fields. In this study, it was observed that the jet undergoes refraction, meaning its initial direction changes when passing through a direct current (DC) magnetic field. This refraction is accompanied by expansion and fluctuations in the jet's mean flow. The degree of refraction was measured using a refractive index (RI), denoted as  $n$ , which was related to the Stuart (magnetic interaction) number  $\mathcal{N}$ . For moderate Stuart numbers ( $\mathcal{N} \leq 0.5$ ), the refraction index followed a simple relationship,  $n \approx 1 - \mathcal{N}$ , regardless of the jet's inclination angle. At higher values ( $\mathcal{N} > 0.5$ ), refraction index varies with inclination due to the development of reverse flow zones adjacent to the main jet, a behavior previously reported by the authors. At certain critical  $\mathcal{N}$  values, full reflection occurs, where the jet cannot penetrate the magnetic field. When the jet is confined by conductive walls, refraction intensifies, leading to earlier full reflection. These findings provide insight into the mechanisms behind the bending and expansion of astrophysical relativistic jets, suggesting that similar magnetic interactions may influence the RJs behavior as they encounter magnetic fields in space.

## 1. Introduction

A turbulent jet of conductive matter undergoes complex transformations when exposed to a strong magnetic field, a phenomenon that plays a significant role across a wide range of scales, from vast astrophysical systems to practical industrial applications.

In astronomy, astrophysical jets — sometimes spanning millions of parsecs — consist of ionized matter emitted as extended beams from high-energy sources, such as supermassive black holes (SMBH) in active galactic nuclei (AGN), quasars, radio galaxies, and their clusters [1]. These jets are highly accelerated and approach the speed of light, becoming relativistic jets (RJs) as they exhibit effects predicted by special relativity [2]. SMBH systems generate the most powerful jets, with a wide range of velocities. For instance, SS 433,

\* Corresponding author.

E-mail address: [abdellah.kharicha@unileoben.ac.at](mailto:abdellah.kharicha@unileoben.ac.at) (A. Kharicha).

the first known relativistic jet source in the Milky Way galaxy, located about 20,000 light-years from Earth, has an average ejection velocity of 0.26 times the speed of light [3].

The relativistic jets emitted by SMBHs remain one of the unresolved mysteries in astrophysics. For example, the SMBH at the center of the Centaurus A galaxy produces two RJs composed of high-energy particles and other material, each extending about 13,000 light-years into space [4]. Some quasars, such as ULAS J1342+0928 [5], Pōniuā'ena [6], and QSO J0313–1806 [7], are among the oldest known objects in the universe, having formed only 600–700 million years after the Big Bang. Even minor advances in understanding the dynamics of these jets can help address some of the most profound questions in physics.

Significant experimental progress relevant to astrophysical magnetohydrodynamics (MHD) has been made through studies of liquid metals, which exhibit high electrical conductivity and low Prandtl numbers, making them comparable to convection phenomena on an interstellar scale [8]. Numerical simulations also play a crucial role in exploring the mechanisms behind RJ emission from AGNs [9]. Recently, researchers such as Mignone et al. [10], Porth and Komissarov [11], Massaglia et al. [12], Wagner et al. [13], and Gourgouliatos and Komissarov [14] have applied the principles and equations of perfect Newtonian magnetohydrodynamics in 3D simulations. These efforts aim to reveal the origins, collimation, acceleration, stability, and feedback mechanisms of these relativistic jets, offering insights into the future of this exciting research field [15,16].

The mechanisms behind the bending of these astro-scaled RJs are not yet well understood. To the authors' knowledge, only a few studies have focused on the bending mechanisms of these kiloparsec-scale structures. This work proposes potential scenarios based on the results obtained, aiming to shed light on this enigmatic phenomenon.

In metallurgy, a submerged jet is often used to supply fresh molten steel during processes like continuous casting [19]. In other fields, such as fusion energy research, jets are commonly used to supply melt during cooling of the protective chamber of fusion reactors [20]. In many processes involving magnetohydrodynamic (MHD) effects, a turbulent jet interacts with an applied magnetic field, which can help reduce jet instabilities [21] and mitigate asymmetric flow patterns [22–24]. This interaction causes the jet to flatten along the magnetic field lines and form reverse zones [25], which can significantly alter the global flow pattern [26]. This phenomenon was first described analytically by Davidson in his work on MHD [27], and later investigated numerically by Kharicha et al. [25] and experimentally by Belyaev et al. [28].

Fig. 1 illustrates the bending of a liquid melt jet under electromagnetic braking (EMBr) during continuous casting, simulated for the LIMMCAST experiment using the GaInSn alloy [17,18]. The melt is introduced through a submerged entry nozzle (SEN), depicted as a tube with two symmetric ports in Fig. 1(a). The magnetic flux density vector field  $\mathbf{B}_0$  is oriented perpendicular to the jet-flow plane, with maximum EMBr power applied at the SEN bottom.

Electromagnetic braking is typically applied locally using a pair of permanent magnets or by introducing the iron cores of an electromagnet to generate a static magnetic field, as illustrated in the schematic in Fig. 1. The distribution of magnetic flux density varies with the gap size between the EMBr poles, transitioning from a Gaussian-type profile in the present example to a step-wise profile as edge effects become more pronounced with smaller gap sizes, discussed later.

The numerical modeling results in Fig. 1(a) show that as the magnetic field strength increases from 0 mT to 441 mT, the impact angle of the initially inclined jet relative to the magnetic field direction also rises. For clarity, Fig. 1(b) shows the spatial evolution of the two jets. Both images utilize contours or isosurfaces of the time-averaged velocity magnitude  $|\mathbf{u}_{\text{avg}}| = 0.3 \text{ m/s}$  to visualize the jets. Consequently, these findings are directly relevant to understanding the MHD phenomena encountered in industrial processes such as continuous casting.

Localized magnetic fields in industrial applications constitute an extensive topic beyond the scope of this manuscript. Nevertheless, a brief analysis of the magnetic field distribution in the central plane between two magnets is provided for context. The Z-component of the  $\mathbf{B}$  field at each point  $(X, Y)$  of the mid-plane  $(Z = 0)$  between the top and bottom surfaces of two magnets consists of their

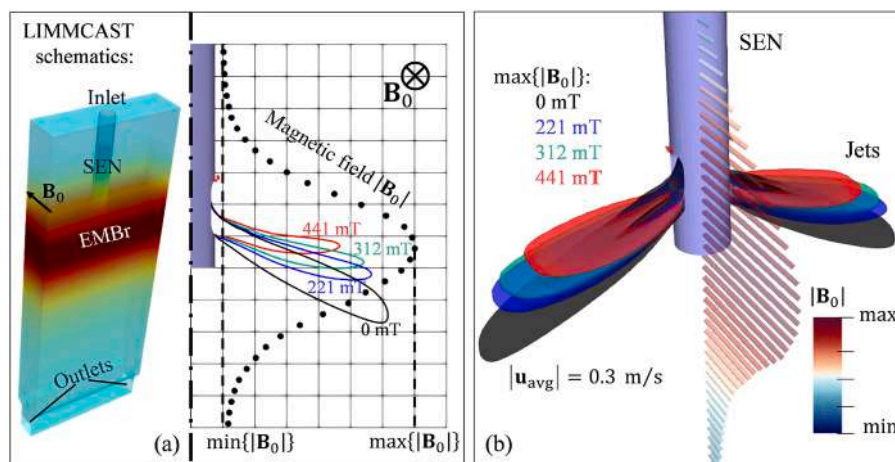


Fig. 1. Bending of the liquid melt jet simulated for the LIMMCAST experiment (HZDR, Germany, [17,18]) under varied EMBr (from 0 mT up-to 441 mT): (a) jet contours in the mid-plane cut and (b) 3D-view of the jet profiles defined by isosurface of  $|\mathbf{u}_{\text{avg}}| = 0.3 \text{ m/s}$ .

superimpose contributions in the form of

$$B_z(X, Y) = \frac{\mu_0 M_s d}{4 \pi} \int_{-\frac{W}{2}}^{\frac{W}{2}} \int_{-\frac{L}{2}}^{\frac{L}{2}} \left( (X - x)^2 + (Y - y)^2 + \left(\frac{d}{2}\right)^2 \right)^{-\frac{3}{2}} dx dy, \tag{1}$$

where  $\mu_0 = 4\pi \times 10^{-7} \frac{T \cdot m}{A}$  is the magnetic permeability of free space;  $M_s$  represents the surface magnetic charge density;  $W$  and  $L$  are the width and length of the magnets;  $d$  corresponds to the distance between magnets (gap size). Although this integral does not have a simple closed-form solution, one can evaluate it numerically. The distribution of  $B_z$  is presented in Fig. 2 for a typical size of the EMBr magnets in the continuous casting process ( $L = 1200$  mm,  $W = 400$  mm).

As shown in Fig. 2(a), a relatively large gap of 160 mm produces a localized Gaussian-type distribution of magnetic flux density. As the gap between the magnets is reduced (Fig. 2(b)-(c)), the distribution transitions to a step-wise profile. Employing a uniform local field in this study simplifies the fundamental investigation by eliminating the effects associated with variations in the magnetic field.

A strong transverse magnetic field can also rotate the flat jet flow plane by  $90^\circ$  within a conductive cavity [29]. The induced current lines close through the liquid bulk, and the resulting Lorentz force not only causes braking effects but can also accelerate the flow by engaging initially stagnant fluid regions [30] and influencing the wave behavior of a free surface [19]. Another significant phenomenon is the formation of quasi-2D turbulence, which has been modeled using large eddy simulations (LES) to accurately capture the MHD flow dynamics, as detailed by Kobayashi in his foundational work [31].

In this novel study, we investigate the influence of an angled magnetic field on a submerged turbulent conductive jet, focusing on its expansion, refraction, and possible complete reflection. A dimensionless numerical analysis is conducted to derive a relationship between the intensity of the applied magnetic field and the degree of the jet’s refraction, referred to as the refractive index. The results of various scenarios are discussed and extended to potential astrophysical applications.

## 2. Numerical model and geometry

As a benchmark case a submerged turbulent jet representing a typical feeding of a conductive fluid was simulated for single flow condition with the Reynolds number (see Equation (2))  $Re=850$  under a wide range of the magnetic field strength. The simulation setup schematic is shown in Fig. 3: the fluid is injected via an extended tube with diameter  $d$  into a domain. The outer boundaries defining the size of the open or confined domain (see details below) are significantly distant from the jet inlet to avoid boundary effects. The back flow is restricted to avoid the numerical instabilities inside the simulation domain. A single direction magnetic field  $\mathbf{B}_0 = \{0 \ B_0 \ 0\}^T$  is applied in the domain locally as a thin layer with the thickness of  $2d$  (see Fig. 3(a)). As one of the defining parameters of the presented study, an inclination angle  $\alpha$ , also named throughout manuscript as the angle of incidence, is introduced between the central axis of a turbulent jet and the local magnetic field region as in Fig. 3(a).

In this study, two scenarios are considered: Case (I) with open boundaries, referred to as the ‘free jet’, and Case (II) with an insulated bottom wall and two conductive side walls, representing a ‘confined jet’ fed into a cavity channel. In the second scenario an

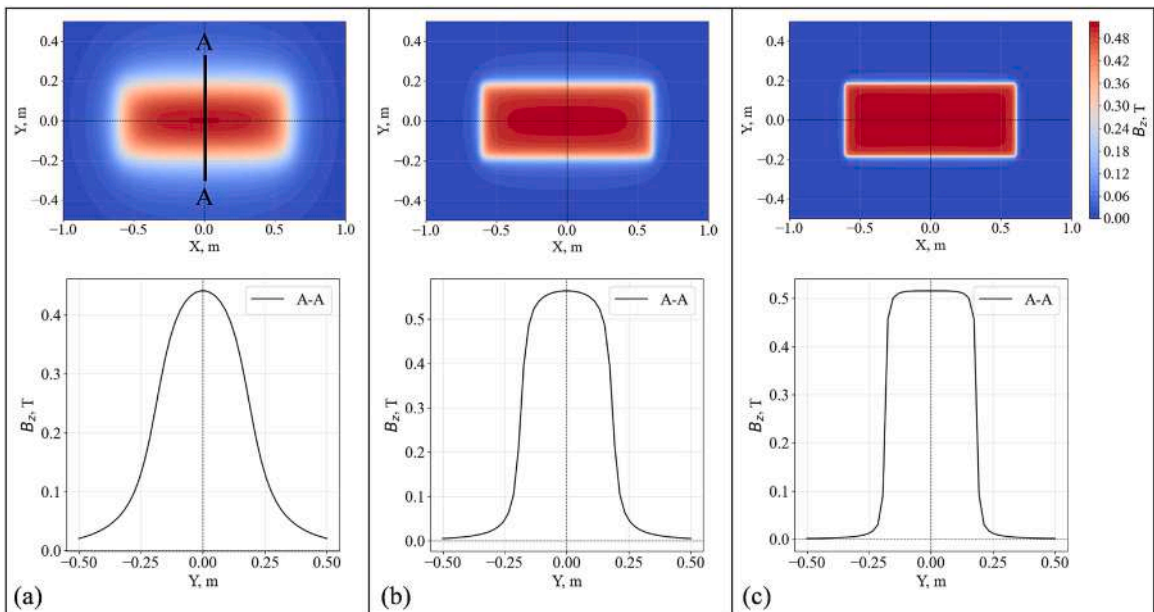


Fig. 2. Magnetic flux density across mid-plane between two permanent magnets with corresponding gap sizes of (a) 160 mm; (b) 80 mm; (c) 40 mm.

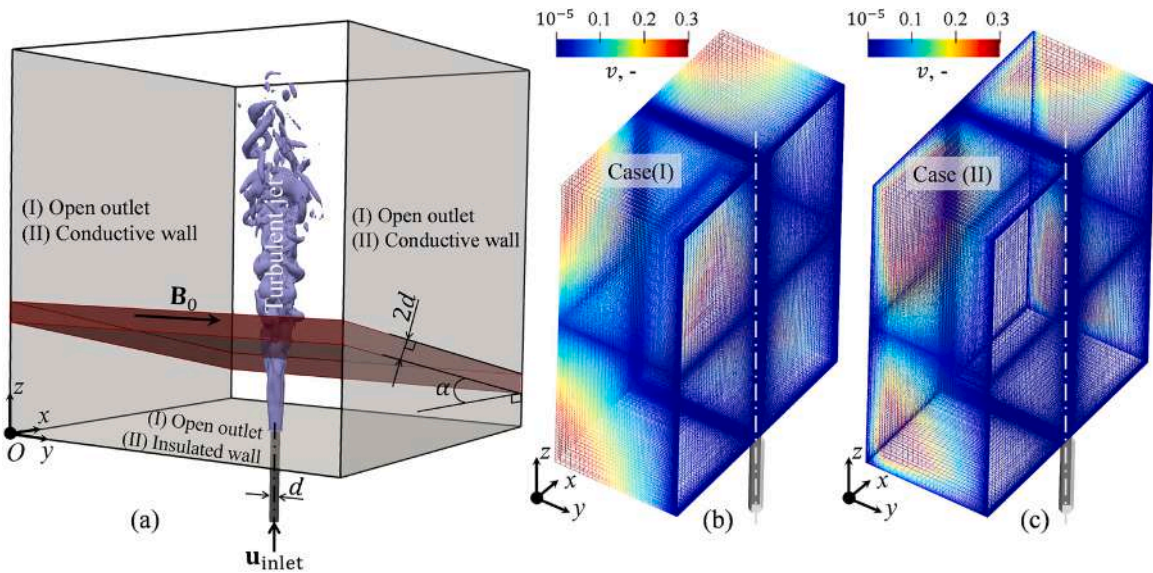


Fig. 3. Simulation setup for Cases (I) and (II): (a) domain geometry and boundary conditions for flow and induced electric current; (b) volume element size ( $v$ ) distribution in the numerical grid for the free-jet Case (I), and (c) for the confined jet Case (II) across half of the full domain.

effect from the conductive side walls (normal to  $B_0$ ) and finite space for the refracting jet are investigated.

Domain size was selected such that the outer boundaries are 20 inlet diameters away from the inlet in both transversal directions  $x$  and  $y$  and 40 diameters in vertical direction  $z$ . Thus, the domain dimensions are  $40 \times 40 \times 40$  characteristic lengths (inlet diameters).

The modeling of the turbulent jet breakup without applied magnetic field was verified in a previous work of the current authors [25] against the experimental work from Todde et al. [32] for the Reynolds number  $Re=2700$ . The mesh convergence studies were presented and discussed aiming to correctly resolve the magnetohydrodynamics phenomena along the jet axis and near the walls. Here in Fig. 4 we present an extended verification for the non-MHD jet against Ref. [32] including  $Re=850, 2700$  and  $4050$ .

Following a mesh convergence study with resolutions of  $150^3, 200^3$  and  $250^3$  elements along the  $x, y,$  and  $z$  axes, respectively, a final numerical grid was designed. Uniform refinement of the entire domain resulted in an inefficient increase in the degrees of freedom of the discretized linear system without adequately resolving the details of the MHD jet. Consequently, localized mesh refinement with cell-size grading was implemented in the jet and applied magnetic field regions, as shown in Fig. 5(a)-(c), as well as adjacent to Hartmann and Shercliff walls, depicted in Fig. 5(d)-(f).

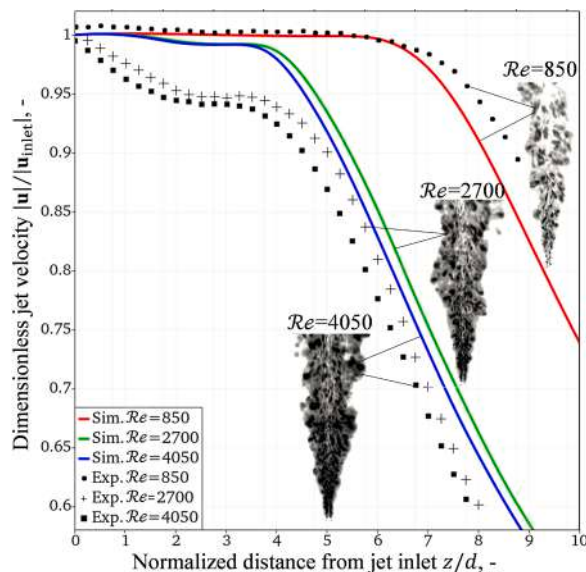


Fig. 4. Decay of the simulated turbulent jet without magnetic field for Reynolds numbers  $Re=850, 2700$  and  $4050$  compared with experimental results of Todde et al. [32].

Mesh grading is indicated in Fig. 5 with brackets and ratio values in blue. The optimized mesh for the present study comprises approximately 10 million volume elements for the free-jet Case (I) with a resolution of  $215^3$  cells, and  $215 \times 245 \times 230$  cells along the  $x$ ,  $y$ , and  $z$  axes for the confined jet Case (II). This configuration effectively resolves the boundary layers, jet breakup, and associated MHD flow phenomena. The distribution of volume element sizes  $v$  is detailed in Fig. 3(b)-(c).

A volume-averaged form of the defining equations were detailed in our previous work Kharicha et al. [25] considering incompressible flow of a conductive liquid under the action of a constant magnetic field. A transition to the non-dimensional form of the basic equations was done by incorporating dimensionless numbers for hydrodynamics and MHD (see Table 1). The corresponding characteristic scales are the inlet velocity magnitude  $|\mathbf{u}_{inlet}|$  for the velocity field, the inlet diameter  $d$  as a characteristic length, and the magnitude of the applied magnetic field  $B_0$  for the magnetohydrodynamic terms. The material properties utilized in Table 1 are density ( $\rho$ ), kinematic viscosity ( $\eta$ ), and electrical conductivity ( $\sigma$ ).

The governing equations for dimensionless variables are listed in Table 2. The mass and momentum conservation laws are given in the form of Navier-Stokes Equations (6)-(7) for dimensionless velocity ( $\hat{\mathbf{u}}$ ) and pressure ( $\hat{p}$ ) fields.

Based on the dimensionless analysis for the low magnetic Reynolds numbers  $\mathcal{R}_{em}$  (see Equation (3)), the induction effects on the external magnetic field  $\mathbf{B}_0$  are negligible. That results in a curl-less formulation for the electric field, and the so-called electric potential  $\varphi$ -method can be applied, resulting in Poisson Equation (8) for the dimensionless electric potential  $\hat{\varphi}$  and magnetic field  $\hat{\mathbf{B}} = \{0 \ 1 \ 0\}^T$ .

The advection-diffusion Equation (9) is introduced for the scalar tracer  $\hat{\xi}$  with a diffusion coefficient  $\hat{D}_\xi$ , which is subsequently employed to analyze complex three-dimensional structures that emerge in the turbulent jet as a consequence of the magnetic field action.

To mimic the turbulent effects, large eddy simulations (LES) were employed. The wall-adapting local eddy-viscosity (WALE) sub-grid scale (SGS) model was used to calculate the Reynolds stresses  $\hat{\tau}_{SGS}$  [33] in Equation (7) since WALE is able to sustain strong grid refinements on complex geometries and correctly predicts the formation of the quasi-2D coherent structures in the MHD flows [31,34].

The Lorentz force  $\hat{\mathbf{F}}_{MHD}$  is incorporated into the momentum conservation Equation (7) based on Equation (11) using either Reynolds and Hartmann numbers (Equations (2) and (4)) or their combination as the interaction (Stuart) number (Equation (5)), which defines the ratio between electromagnetic and inertial forces. In the presented study hereinafter, we employ the interaction number  $\mathcal{N}$

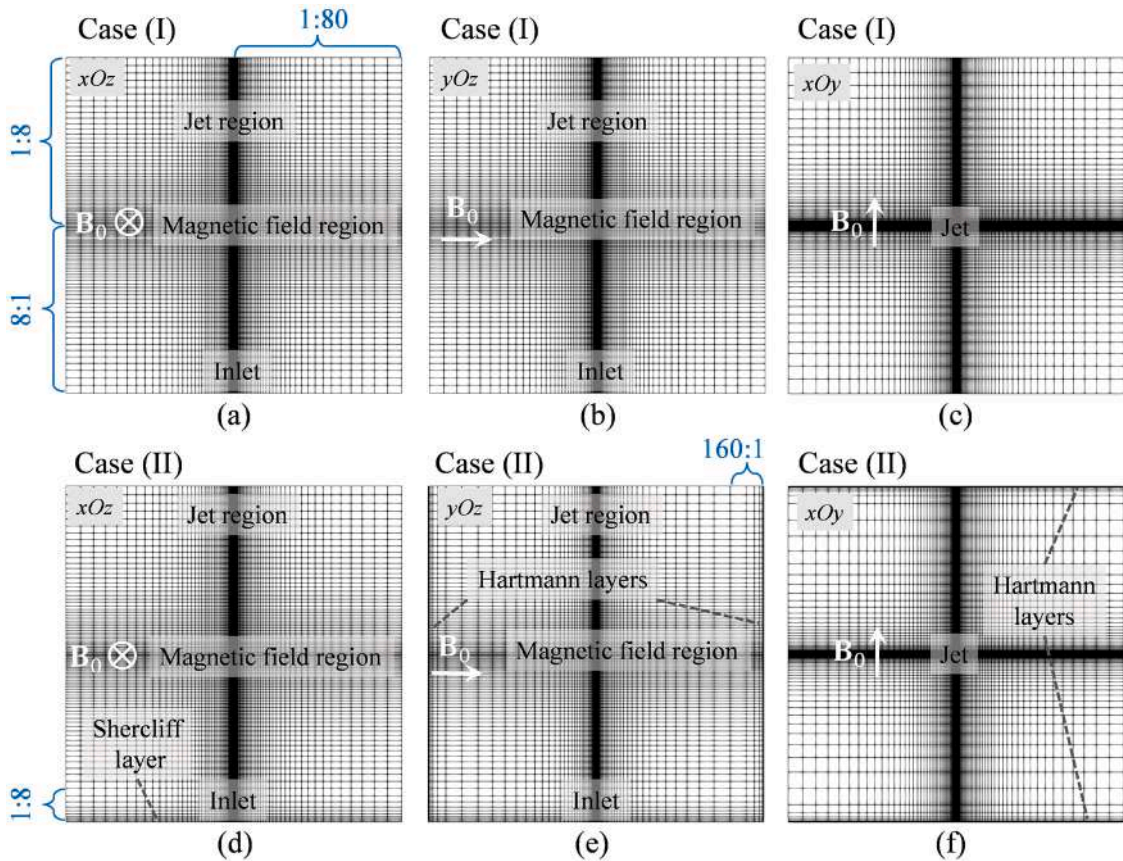


Fig. 5. Schematics of numerical mesh refinement on the Cartesian planes  $xOz$ ,  $yOz$ , and  $xOy$ . Panels (a)–(c) depict Case (I), while (d)–(f) illustrate Case (II). The corresponding cell-grading ratios for the numerical grid regions are highlighted in blue.

**Table 1**  
Dimensionless numbers in hydrodynamic and MHD models.

Reynolds number:	$Re = \frac{ \mathbf{u}_{inlet}  \cdot d}{\eta}$	(2)
Magnetic Reynolds number:	$Re_m =  \mathbf{u}_{inlet}  \cdot d \cdot \mu_0 \cdot \sigma$	(3)
Hartmann number:	$Ha = B_0 \cdot d \cdot \sqrt{\sigma/\rho \cdot \eta}$	(4)
Interaction (Stuart) number:	$\mathcal{N} = \frac{d}{ \mathbf{u}_{inlet} } \cdot \frac{\sigma \cdot (B_0)^2}{\rho} = \frac{Ha^2}{Re}$	(5)

**Table 2**  
Volume-average equations of numerical model in dimensionless form.

<b>Conservation laws</b>		
Mass:	$\nabla \cdot \hat{\mathbf{u}} = 0$	(6)
Momentum:	$\frac{\partial \hat{\mathbf{u}}}{\partial \hat{t}} + \nabla \cdot (\hat{\mathbf{u}} \otimes \hat{\mathbf{u}}) = -\nabla \hat{p} + \frac{1}{Re} \nabla^2 \hat{\mathbf{u}} - \nabla \cdot \hat{\tau}_{SGS} + \hat{\mathbf{F}}_{MHD}$	(7)
Electric potential:	$\nabla^2 \hat{\varphi} = \nabla \cdot (\hat{\mathbf{u}} \times \hat{\mathbf{B}})$	(8)
Passive scalar tracer:	$\frac{\partial \hat{\xi}}{\partial \hat{t}} + \nabla \cdot (\hat{\mathbf{u}} \hat{\xi}) - \nabla \cdot \hat{D}_{\xi} \nabla \hat{\xi} = 0$	(9)
<b>Closure equations</b>		
Current density:	$\hat{\mathbf{j}} = -\nabla \hat{\varphi} + \hat{\mathbf{u}} \times \hat{\mathbf{B}}$	(10)
Lorentz force:	$\hat{\mathbf{F}}_{MHD} = \frac{Ha^2}{Re} (\hat{\mathbf{j}} \times \hat{\mathbf{B}}) = \mathcal{N} (\hat{\mathbf{j}} \times \hat{\mathbf{B}})$	(11)
Tracer diffusivity:	$\hat{D}_{\xi} = \frac{\eta_{eff}}{Pr_{\xi} \cdot  \mathbf{u}_{inlet}  \cdot d}$	(12)
<b>Flow characteristics</b>		
Q-criterion:	$\mathcal{Q}_{crit} = \frac{1}{2} [(\text{tr}(\nabla \hat{\mathbf{u}}))^2 - \text{tr}(\nabla \hat{\mathbf{u}} \cdot \nabla \hat{\mathbf{u}})]$	(13)

for the results analysis, since it gives an estimate of the relative importance of a magnetic field on flows of conducting fluids, e.g. in fusion reactors, steel casters or plasmas.

A conservative scheme, published elsewhere by Ni et al. [35], was employed to discretize the Lorentz force in the momentum Equation (7): the body force  $\hat{\mathbf{F}}_{MHD}$  was reconstructed using Green-Gauss-like surface integration. The checkerboarding of the numerical solution, which is notorious for occurring on collocated grids [36], was eliminated through Rhie-Chow interpolation [37].

A second order temporal and spatial discretization was employed, along with the monotonic upstream-centered scheme for conservation laws (MUSCL) total variation diminishing (TVD) scheme [38], to model the convective term in the momentum Equation (7). The Courant–Friedrichs–Lewy (CFL) condition [39] was maintained with a threshold of 1 because comparisons with Todde’s [32] experimental results showed that exceeding this threshold led to excessive numerical diffusion, resulting in deviations from the experimental measurements.

To accurately capture sufficient temporal statistics of the velocity field, the simulation’s time scale resolution was ensured by monitoring the dimensionless integral kinetic energy  $K = \int \int \int \frac{\hat{\mathbf{u}}^2}{2} dv$  and Joule dissipation  $J = \int \int \int \frac{\hat{\mathbf{j}}^2}{2} dv$ . A sliding-average filter was applied, as displayed in Fig. 6, to estimate the amount of the resolved significant fluctuation cycles in the monitored parameters, thereby ensuring that the data collected is statistically meaningful.

The in-house solver including turbulent flow and the MHD model was developed using finite volume method (FVM) framework of

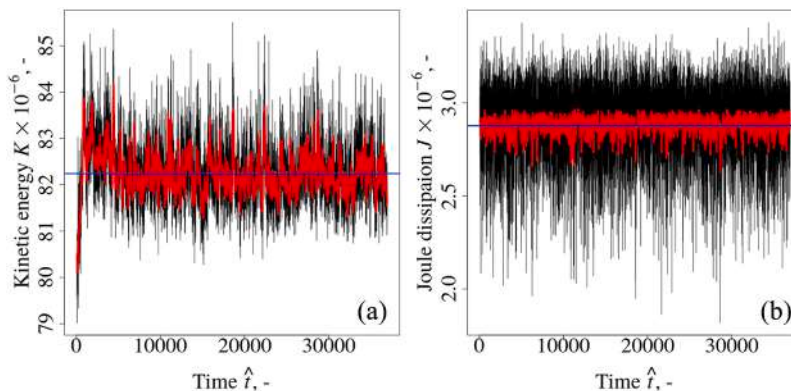


**Fig. 6.** Temporal evolution of the dimensionless integral (a) kinetic energy  $K$  and (b) Joule dissipation  $J$ . The black curves represent the raw data, while the red curves depict the corresponding sliding average computed using a 500-point filter.

the open-source CFD package OpenFOAM® [40].

### 3. Simulation results

The damping of the jet by the sudden impact of the local magnetic field region, normal to the jet axis, is studied initially. In our previous study [25] the Joule dissipation for a submerged jet was compared with the theoretical derivations by Davidson [27]. We highly encourage the reader to follow [25], where the conclusions are briefly summarized as follows: (i) the non-MHD turbulent jet develops symmetrically in all directions; (ii) when a transverse magnetic field is applied, the conductive jet becomes significantly flatter in the direction perpendicular to the magnetic field; (iii) strong recirculation zones develop and stretch along the growing applied magnetic field; (iv) the transient flow shows the oscillations and instabilities. Based on the referenced study the decay in the uniform transverse magnetic field was derived to behave as

$$\hat{u}_z \sim \exp\left(-\sqrt{\mathcal{N}} \cdot \hat{z}\right). \tag{14}$$

Fig. 7 displays the decay of a free turbulent jet (based on the time-averaged dimensionless velocity  $\hat{u}_{avg}$ ) when a magnetic field is absent and when it is applied normal to the jet’s axis. The evolution of a jet shape is shown next to the corresponding decay curves. As estimated from plotted data, the jet is damped at the exit of the MHD braking zone by an additional 4.9 % comparable to the non-MHD case for a low value of  $\mathcal{N}=0.05$ , by 38.6 % for larger  $\mathcal{N}=0.5$  and by 57.6 % for  $\mathcal{N}=0.75$ . For the interaction number  $\mathcal{N} \geq 1$  the turbulent jet is completely damped before crossing the magnetic field area. A slight kink observed in the velocity magnitude curve downstream of the applied magnetic field is a result of the complex flow pattern and reverse fluid entrainment (see Fig. 8), caused by recirculation zones formed within the magnetic field region [25].

The jet structure below the magnetic field is changed as well due to occurrence of the “reflected” side jets oriented downstream in Fig. 8.

In Fig. 9 the time-averaged velocity magnitude and vector field is used to represent the inclined jet evolution under a growing magnetic field.

For moderate values of  $\mathcal{N}=0.281$  and  $\mathcal{N}=0.5$  (Fig. 9(a)-(b)), the inclined jet becomes diffuse and undergoes slight refraction due to the Lorentz force after passing through the magnetic field region. As can be seen from the performed numerical simulations, a backward reversed jet develops below the magnetic field zone. Its refraction angle grows together with the refraction angle of the main jet for stronger magnetic flux at  $\mathcal{N}=0.75$  (Fig. 9(c)). The second jet below the magnetic field area flows in the opposite direction to the main jet. Then the flow pattern significantly restructures into two reflected jets below the magnetic field region (Fig. 9(d)-(e)). For  $\mathcal{N}=1$  the bottom-right reflected part of the jet constantly oscillates as marked in Fig. 9(d). Its transient dynamic is discussed later using instantaneous velocity field. The front reversed jet stabilizes at a stronger magnetic field for  $\mathcal{N}=1.125$  (Fig. 9(e)) and deviates rightwards away from the turbulent jet axis. Next, the refraction angle above the applied magnetic field area becomes equal to  $90^\circ$  (Fig. 9(e)) and at some critical magnetic strength the jet is fully blocked (Fig. 9(f)), being forced to travel below the applied zone.

In Fig. 10 the damping of the free jet’s velocity along its axis is compared for the cases  $\alpha=0^\circ$  and  $\alpha=15^\circ$ . It is observed that inside the magnetic field region a very similar decay rate happens, and the curves are very similar. It should be noted that the effective thickness

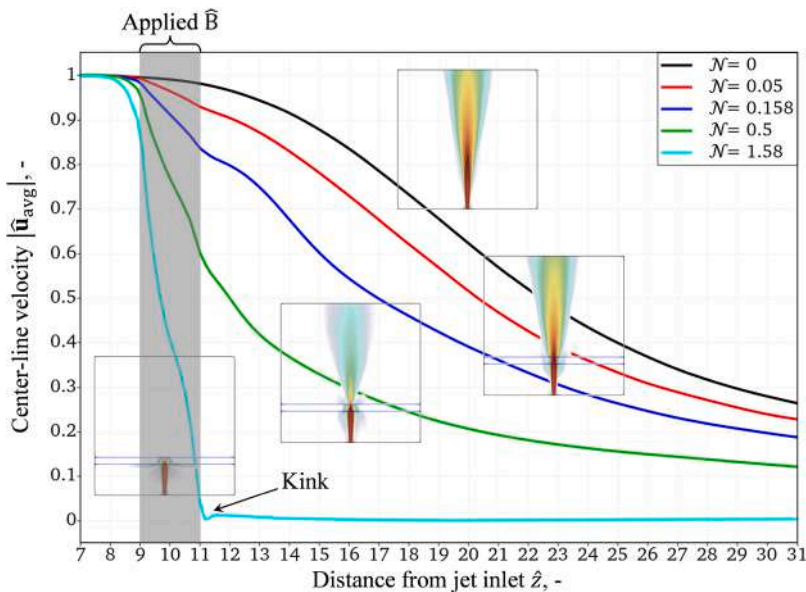


Fig. 7. Damping of a turbulent jet across the horizontal ( $\alpha=0^\circ$ ) DC magnetic field region (marked in grey) for the interaction number values  $\mathcal{N}=0, 0.05, 0.158, 0.5$  and  $1.58$ .

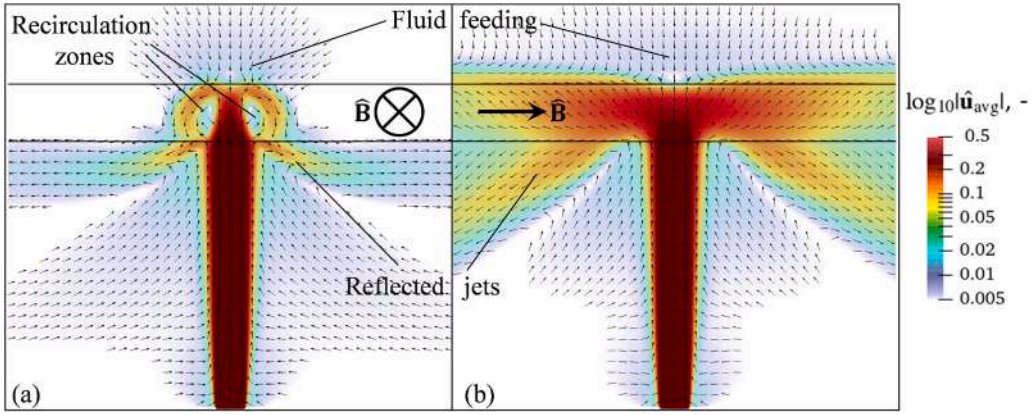


Fig. 8. Jet structure in (a) normal and (b) parallel planes to magnetic field  $\hat{\mathbf{B}}$  ( $\alpha=0^\circ$ ) for the interaction number  $\mathcal{N}=1.58$ .

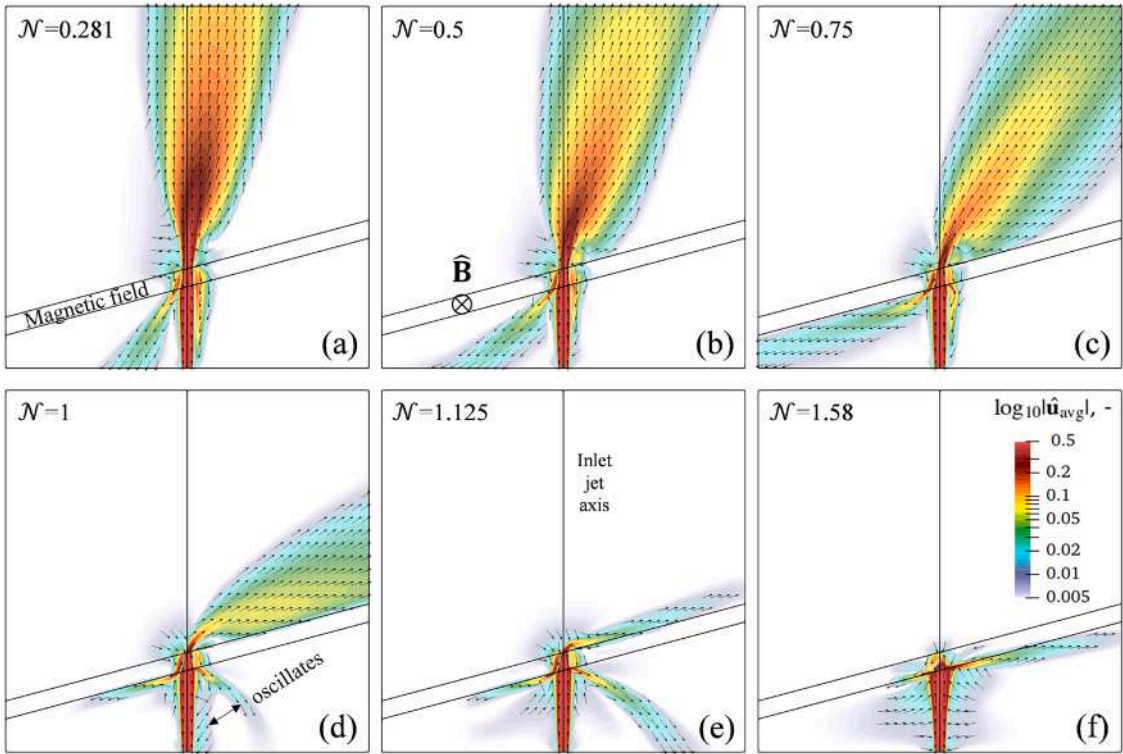


Fig. 9. Turbulent jet in the open domain under the inclination by  $\alpha=15^\circ$ : time-average flow velocity field in the midplane normal to the  $\hat{\mathbf{B}}$  field for the interaction number  $\mathcal{N}$  values (a)  $\mathcal{N}=0.281$ , (b)  $\mathcal{N}=0.5$ , (c)  $\mathcal{N}=0.75$ , (d)  $\mathcal{N}=1$ , (e)  $\mathcal{N}=1.125$ , and (f)  $\mathcal{N}=1.58$ .

of the magnetic field region depends on the inclination angle  $\alpha$ , more precisely it is proportional to  $\cos^{-1}\alpha$ . For the considered inclination angles, the effective thickness equals 1.0154, 1.035, and 1.064 times the original magnetic region thickness ( $2d$ ) for  $\alpha=10^\circ$ ,  $15^\circ$ , and  $20^\circ$ , respectively. Thus, the deviations in results for the inclination angles  $\alpha=0^\circ$ ,  $10^\circ$ ,  $15^\circ$ , and  $20^\circ$  within the braking zone are caused by variations in thickness. However, there is a significant difference in the decay along the axis after passing the magnetic zone since the inclined jet refracts in comparison to the vertical one.

The performed studies reveal a complex spatial structure of the refracted conductive jet. Therefore, to visualize the development of the jet in 3D, a passive scalar tracer  $\hat{\xi}$  was numerically injected into the simulation domain at the inlet. The transport of  $\hat{\xi}$  is described by advection-diffusion Equation (9). The dimensionless tracer diffusivity  $\hat{D}_\xi$  is calculated according to Equation (12) based on the effective kinematic viscosity  $\eta_{\text{eff}}$  of the real flow, velocity and length scales  $|\mathbf{u}_{\text{inlet}}|$  and  $d$ , as well as on the Prandtl number for the tracer  $\hat{\xi}$  which was taken for simplicity to be  $\text{Pr}_\xi = 1$ .

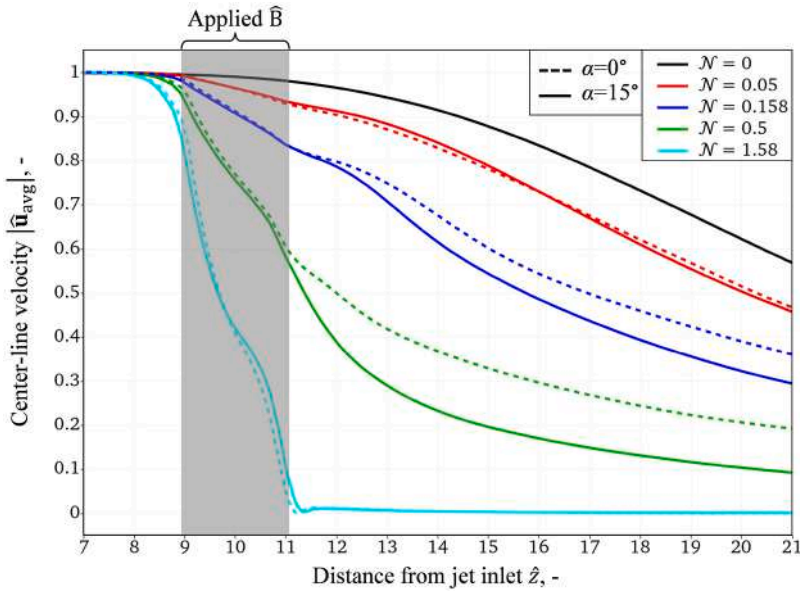


Fig. 10. Damping of a turbulent jet across the inclined ( $\alpha=15^\circ$ ) DC magnetic field region, for the interaction number values  $\mathcal{N}=0, 0.05, 0.158, 0.5$  and 1.58. Dashed lines correspond to the horizontal ( $\alpha=0^\circ$ ) magnetic field case.

The corresponding 3D isocontours of the instantaneous distribution of the scalar tracer  $\hat{\xi}$  are presented in Fig. 11–13 for the interaction numbers  $\mathcal{N}=0.75, 1$  and 1.58. The distribution is displayed at the dimensionless time  $\hat{t} = 1000$ , defined as  $\hat{t} = d / |\mathbf{u}_{\text{inlet}}|$ , when the passive scalar tracer  $\hat{\xi}$  has sufficiently propagated throughout the domain. To ensure consistent color saturation across regions with different flow velocities,  $\hat{\xi}$  is scaled to a range from 0 to 0.5. Brighter areas in Figs. 11–13 indicate higher tracer concentrations and correspond to faster flow regions, such as jets and recirculation zones. In contrast, darker regions represent lower concentrations, typically associated with slower flow structures.

In the first pictures the turbulent structure is analyzed for the interaction number  $\mathcal{N}=0.75$  (see Fig. 11). The general overview in Fig. 11(a) indicates the refracted main jet, a small reverse flow zone formed inside the magnetic field region and two side reverse jets as well as one directed opposite to the main jet. To understand in more detail, the side and top views are displayed in Fig. 11(b)-(c). Two reverse flow zones, marked with dashed circular arrows in Fig. 11(b), were carefully investigated in our previous work Kharicha et al. [25]. They are clearly seen due to the specific distribution of the tracer  $\hat{\xi}$ . The direction of the reversed side and opposite jets becomes clearer from this side projection supplemented by the top view in Fig. 11(c).

The jets transformation with the increase of the magnetic field strength is presented in Fig. 12 for  $\mathcal{N}=1$ . The main jet becomes strongly refracted by a significant angle. Three reversed jets (as in previous case for  $\mathcal{N}=0.75$ ) are now supplemented by the fourth reversed jet in the direction of the main jet. As analyzed for  $\mathcal{N}=1$  using the instantaneous velocity distribution in Fig. 14 the fourth jet sometimes flows parallel to, and in the opposite direction to, the injected stream or appears as a separate reversed jet. The reverse flow zones evolve into elongated vortex tubes under stronger MHD forces (see Fig. 12(a)). They promote secondary flow above the  $\hat{\mathbf{B}}$  region,

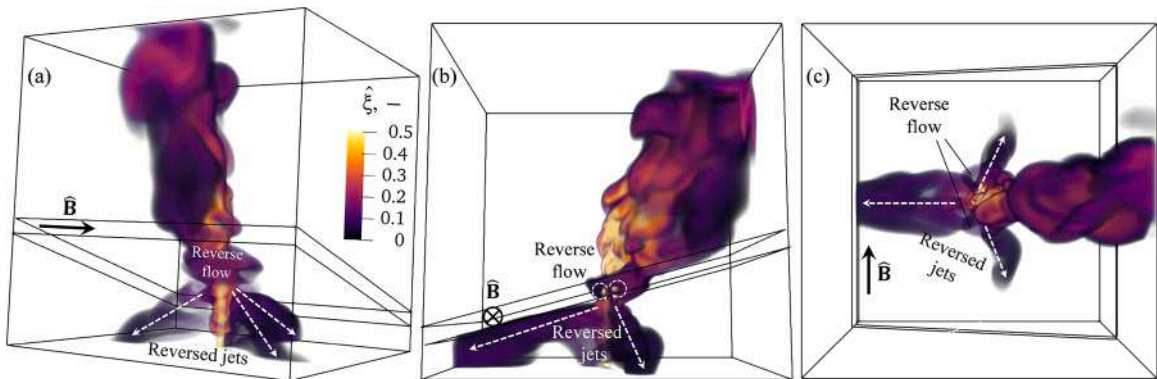


Fig. 11. 3D isocontours of the scalar tracer distribution at  $\hat{t} = 1000$  for a turbulent jet traveling across inclined magnetic field ( $\alpha=15^\circ, \mathcal{N}=0.75$ ): (a) frontal projection; (b) side view; (c) top view.

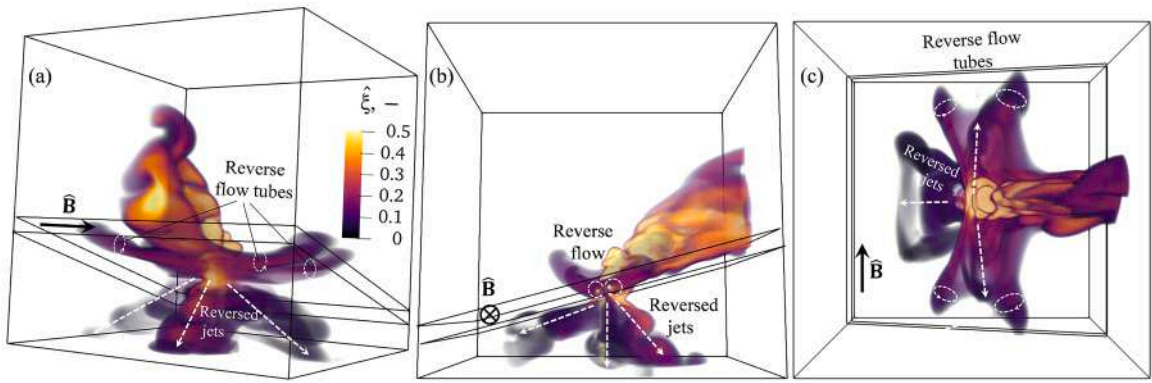


Fig. 12. 3D isocontours of the scalar tracer distribution at  $\hat{t} = 1000$  for a turbulent jet traveling across inclined magnetic field ( $\alpha=15^\circ$ ,  $\mathcal{N}=1$ ): (a) frontal projection; (b) side view; (c) top view.

as shown in Fig. 12(b). The opposite reversed jet in Fig. 12(b)-(c) becomes wider but shorter and slower (see Fig. 9(d)) in comparison to the results in Fig. 11.

For the highest interaction number value of  $\mathcal{N}=1.58$  in Fig. 13(a) some secondary vortex structures above the magnetic field region are generated due to the strong reverse flow zone inside the magnetic field region. The main stream and the side reversed jets become fully reflected and flow completely underneath the magnetic field (see Fig. 13(b)). The corresponding reversed jet in comparison to the main jet becomes almost “annihilated”, according to the definition from Davidson [41]. Despite being observed, velocity magnitudes significantly drop according to Fig. 9(f). The flow in the reversed jet is slowly spreading in a fan-like direction, as shown by the top view in Fig. 13(c).

The important phenomena, revealed by the tracer dynamics, are the expansion of the jet after refraction and consequent hydrodynamic instability and oscillation of the mean flow. Readers are invited to explore the supplementary animations, Video\_S1-S3.mp4, which depict the jet dynamics through passive scalar tracing.

The performed analysis of the complex 3D structure provides a further insight into the oscillations of the front reversed jets, which was revealed in Fig. 9(d). For that purpose, the dynamics of the refracted jet at interaction number  $\mathcal{N}=1$  and  $\hat{\mathbf{B}}$  inclined by  $\alpha=15^\circ$  was studied and presented in Fig. 14.

At the dimensionless time instant of  $\hat{t}=4800$  (Fig. 14(a)-(b)) the front and side reversed jets (seen in Fig. 12(a)-(b)) flow in the opposite direction to the main submerged jet below the magnetic field. With the course of time at  $\hat{t}=13,170$  (Fig. 14(c)-(d)) the reversed side jets separate from the main liquid stream. Furthermore, the front jet separates at  $\hat{t}=19,860$  (Fig. 14(e)-(f)), and the recirculation zones are formed between side and front reversed jets, marked with the dashed circular arrows in Fig. 14(f). The described phenomenon repeats periodically. The separation of the reversed front and side jets becomes stable for  $\mathcal{N}>1$ . Readers are encouraged to view the supplementary animation, Video\_S4.mp4, to observe the complete jet dynamics.

Fig. 15 supplements the 2D results presented in Fig. 9 in main cross-sections by 3D representation of the velocity field streamlines, jet shape with its stretching along the magnetic field and with the induced electric current density lines for most representative cases with the interaction number  $\mathcal{N}=0.158$ , 0.75 and 1.58. These illustrations give us new insights, that along with the side jets below magnetic field in Fig. 9(a) additional reflected jets develop to the sides from the main jet in the parallel to the magnetic field direction (Fig. 15(d)-(e)). This featured flow could not be detected from mid-cuts of the simulation domain. It is also seen that the reverse zones

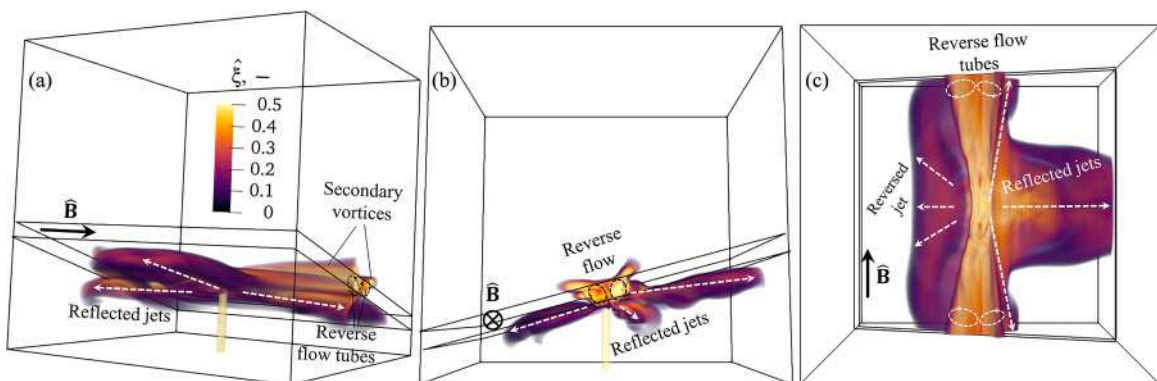
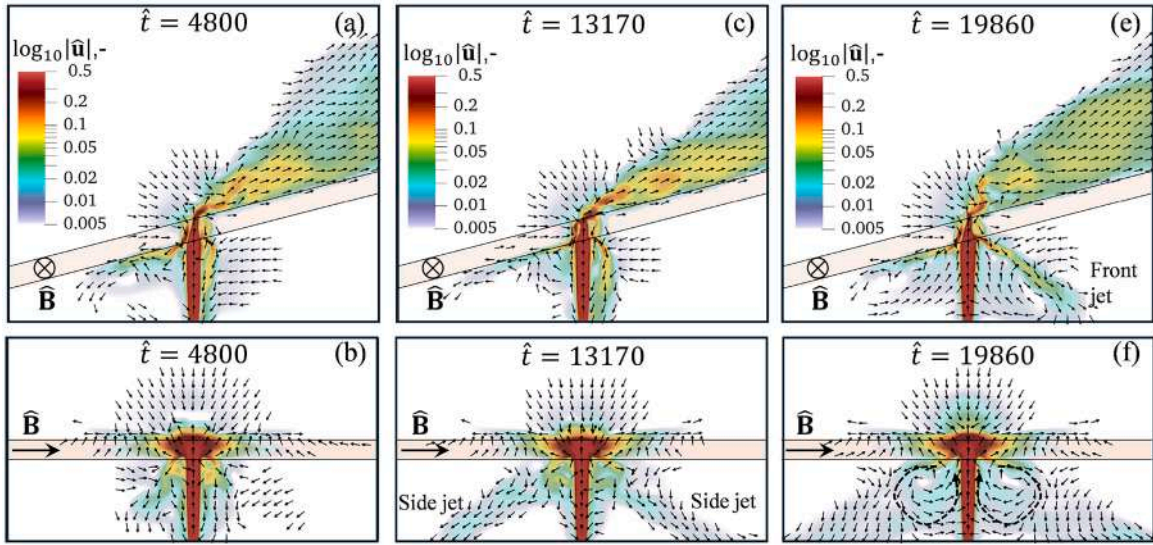


Fig. 13. 3D isocontours of the scalar tracer distribution at  $\hat{t} = 1000$  for a turbulent jet traveling across inclined magnetic field ( $\alpha=15^\circ$ ,  $\mathcal{N}=1.58$ ) (a) frontal projection; (b) side view; (c) top view.



**Fig. 14.** Instantaneous velocity of a turbulent jet under action of the magnetic field  $\hat{\mathbf{B}}$  inclined by  $\alpha=15^\circ$  for the interaction number  $\mathcal{N}=1$  in the midplane cuts normal to  $\hat{\mathbf{B}}$  (top row) and parallel to  $\hat{\mathbf{B}}$  (bottom row) at the dimensionless time instants (a)-(b)  $\hat{t}=4800$ ; (c)-(d)  $\hat{t}=13,170$ ; and (e)-(f)  $\hat{t}=19,860$ .

completely stretch along the magnetic lines and become the dominant direction of the fluid motion (Fig. 15(g)-(h)).

The evolution of the induced current density loops starts as they concentrate at low  $\mathcal{N}$  around the zone where the main jet interacts with the magnetic field (Fig. 15(c)); then the significant flux of the e-current distributes along the magnetic transversal direction (Fig. 15(f)) and at the case of the deflected jet almost completely goes out through the sides (Fig. 15(i)).

The localized distribution of the induced electric current component  $\hat{\mathbf{J}}_{xz}$  normal to the magnetic field  $\hat{\mathbf{B}}$  is displayed in Fig. 16. In our previous study [25] it was highlighted that the most important phenomena of the jet's stretching by the Lorentz force along the magnetic field lines and formation of the corresponding reverse flow zones are happening in the direction normal to  $\hat{\mathbf{B}}$  plane. In the example case for the angle of incidence  $\alpha=15^\circ$  at the interaction number  $\mathcal{N}=0.75$ , the induced electric density is strongest inside the applied magnetic field region, where it is generated by the jet interaction with  $\hat{\mathbf{B}}$ . The e-current goes in concentric loops around the bottom central entrance point of the jet and at the top shifted exit central point changing its coherent flow direction at the central plane of the magnetic field zone.

As revealed in previous studies [19,25,31,34], the turbulence is strongly affected by the action of MHD forces. The second invariant of the velocity gradient tensor field  $\mathcal{C}_{crit}$ , the so-called Q-criterion, was used according to Equation (13) as a commonly applied flow characteristic to visualize coherent turbulent structures [42,43].

A consequent evolution of a turbulent jet is illustrated in Fig. 17 with growing interaction number  $\mathcal{N}$ . As can be seen, developed coherent 3D structures, traveling along jet vertical axis, are observed both for the no magnetic field case (Fig. 17(a)) and very low interaction number  $\mathcal{N}=0.05$  (Fig. 17(b)). For the latter case a small zone of a reverse flow occurs inside magnetic field region. With further increase of the magnetic field strength (see Fig. 17(c)-(f)) the reverse flow zones start to elongate along magnetic field lines. The reversed jet, opposite to the main jet, is formed with the horseshoe-type coherent structures. Interestingly, these bowed vortices, generated by MHD forces, keep their alignment even after leaving the magnetic field region.

Furthermore, the turbulent eddies of the main jet become coarser at higher  $\mathcal{N}$  due to the re-laminarization of the flow. Moreover, when the interaction number enters the range  $\mathcal{N} \geq 1$ , (Fig. 17(g)-(k)) they transform from anisotropic 3D structures to tubes (aligned with the magnetic field) or to horseshoe vortices with a plane of symmetry normal to  $\hat{\mathbf{B}}$ . They maintain their characteristic shape outside of the magnetic field, as emphasized before.

Although the presented  $\mathcal{N}$  values are distributed almost linearly, it should be noted that, the dynamics of the turbulence damping is much stronger for interaction number larger than  $\mathcal{N}=0.5$ .

## 4. Discussions

### 4.1. Calculation of the jet's refraction angle

The refraction of the investigated jet can be likened to the refraction and reflection phenomena observed in optics. The authors use this qualitative analogy to quantify the jet's refraction. As illustrated earlier in Fig. 9, the refraction angle of a turbulent jet increases as it passes through the region of the applied magnetic field, with the angle growing in response to increasing magnetic field intensity. In this section, we quantify the refraction angle based on the calculation algorithm outlined in Fig. 18. Unlike a light beam passing

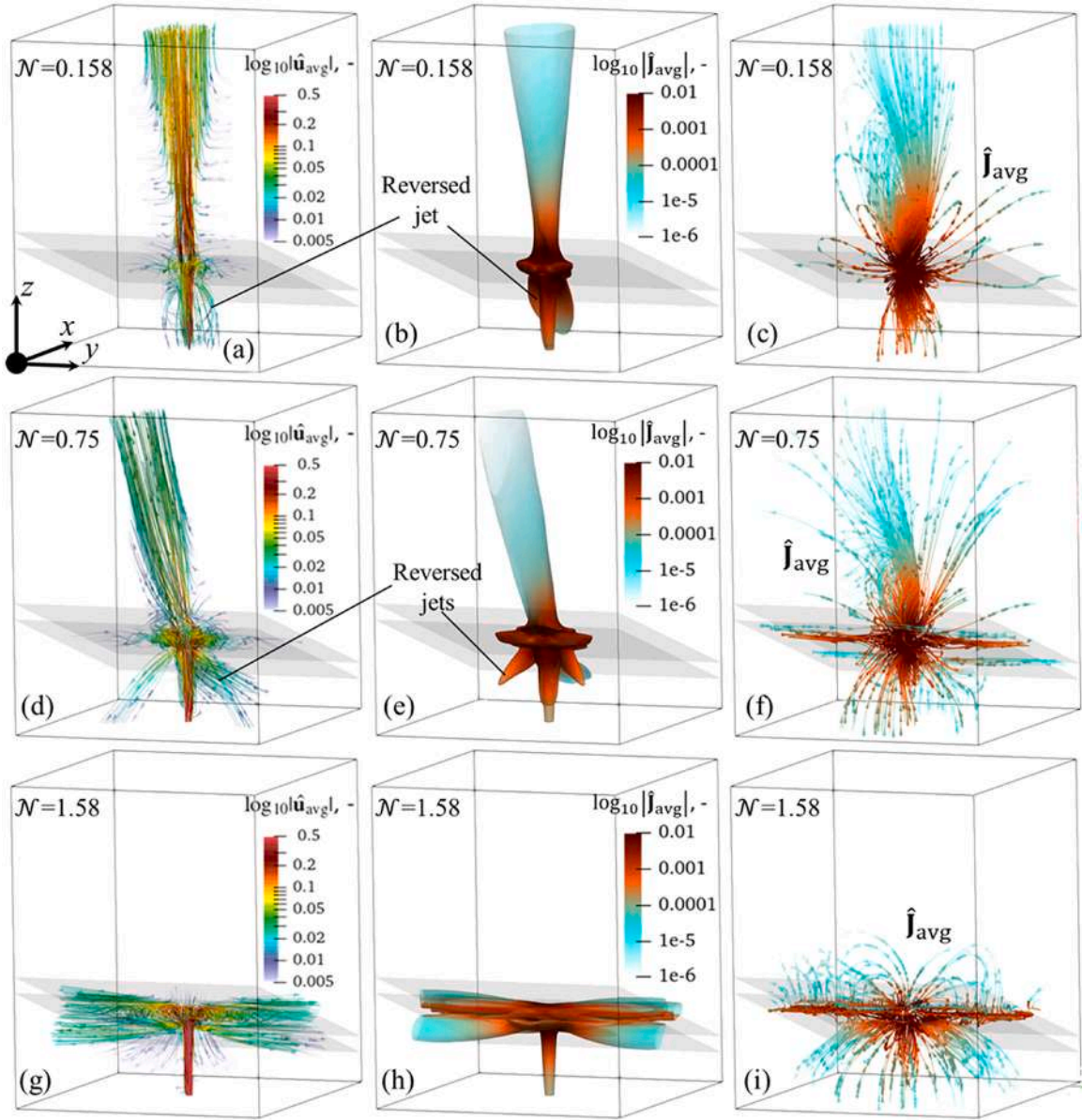


**Fig. 15.** Time-averaged streamlines (left column), jet shape (isosurface of  $|\hat{\mathbf{u}}_{\text{avg}}| = 0.025$ , middle column) and induced e-current lines (right column) under the inclination by  $\alpha=15^\circ$  for the interaction number values (a)-(c)  $\mathcal{N}=0.158$ , (d)-(f)  $\mathcal{N}=0.75$  and (g)-(i)  $\mathcal{N}=1.58$ .

through a prism, the refracted jet exhibits a more complex structure due to the formation of reverse flow zones and its flattening under the influence of the magnetic field. However, a detailed analysis conducted during this study revealed that, after the development of a transition zone (indicated by the grey rectangle in Fig. 18(a)), the refracted jet adopts a single dominant direction.

To track the dominant direction, vorticity of the time-averaged velocity was estimated as  $\hat{\omega}_{\text{avg}} = \nabla \times \hat{\mathbf{u}}_{\text{avg}}$  along the isolines of  $|\hat{\mathbf{u}}_{\text{avg}}|$  (see Fig. 18(a)). The lowest vorticity values (ideally  $|\hat{\omega}_{\text{avg}}| = 0$ ) assist in identifying the jet's axis and its dominant direction, marked with the dashed line in Fig. 18(a). Next, one estimates the refraction velocity vector  $\hat{\mathbf{u}}_{\text{avg}}^{\text{ref}}$  at the jet's axis point  $(\hat{x}_{\text{ref}}; \hat{z}_{\text{ref}})$ . The diagram in Fig. 18(b) displays all isoline points in relation to vorticity magnitude  $|\hat{\omega}_{\text{avg}}|$  along with the calculated velocity angle  $\gamma$  based on the following formula:

$$\gamma(\hat{x}, \hat{z}) = \arctan \frac{\hat{u}_x(\hat{x}, \hat{z})}{\hat{u}_z(\hat{x}, \hat{z})}. \tag{15}$$

The refraction angle  $\gamma_{\text{ref}}$  is then found at location  $(\hat{x}_{\text{ref}}; \hat{z}_{\text{ref}})$  corresponding to the lowest vorticity  $|\hat{\omega}_{\text{avg}}|$  values as marked in the left side of Fig. 18(b).

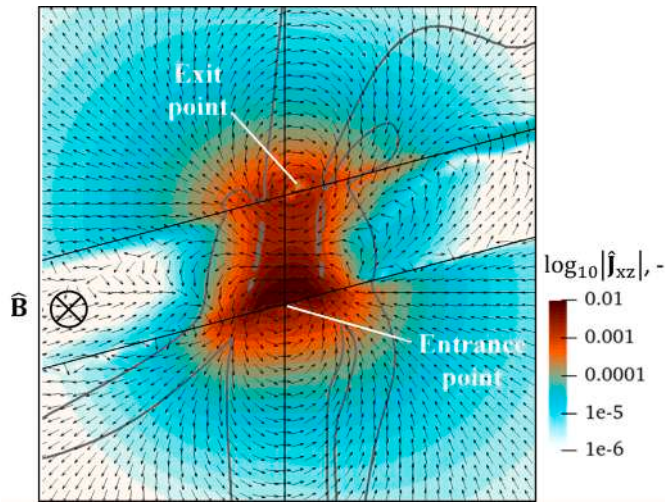


Fig. 16. Distribution of the induced electric current component  $\hat{J}_{xz}$  normal to the magnetic field  $\hat{B}$  for the inclination angle  $\alpha=15^\circ$  and the interaction number  $\mathcal{N}=0.75$ . Jet borders are in grey defined by isocontours of time-averaged velocity magnitude  $|\hat{u}_{avg}| = 0.025$ .

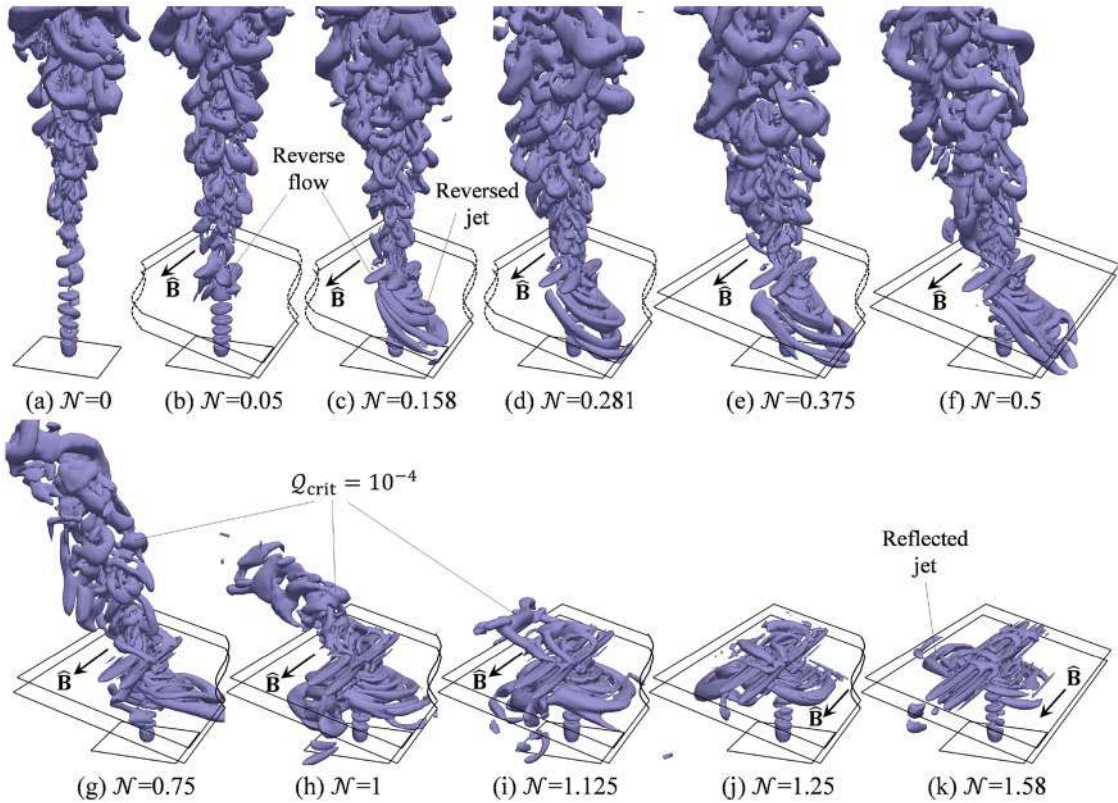


Fig. 17. Evolution of the jet's turbulent structures defined by the isosurface of the Q-criterion value  $\mathcal{Q}_{crit} = 10^{-4}$  under the inclined magnetic field  $\hat{B}$  ( $\alpha=15^\circ$ ) for the consecutive growth of the interaction number: (a)  $\mathcal{N}=0$  (no magnetic field); (b)  $\mathcal{N}=0.05$ ; (c)  $\mathcal{N}=0.158$ ; (d)  $\mathcal{N}=0.281$ ; (e)  $\mathcal{N}=0.375$ ; (f)  $\mathcal{N}=0.5$ ; (g)  $\mathcal{N}=0.75$ ; (h)  $\mathcal{N}=1$ ; (i)  $\mathcal{N}=1.125$ ; (j)  $\mathcal{N}=1.25$ ; (k)  $\mathcal{N}=1.58$ .

Next, the refractive index of a turbulent jet under the applied inclined magnetic field was investigated for the different interaction number  $\mathcal{N}$  values. Theoretically for the light or waves propagation through the boundary of two isotropic media, the angles of incidence  $\alpha$  and refraction  $\gamma$  are related according to the Snell's law of refraction [44]. Expressed through the refractive indices of corresponding two media  $n_\alpha$  and  $n_\gamma$ , the formula for Snell's law is obtained:

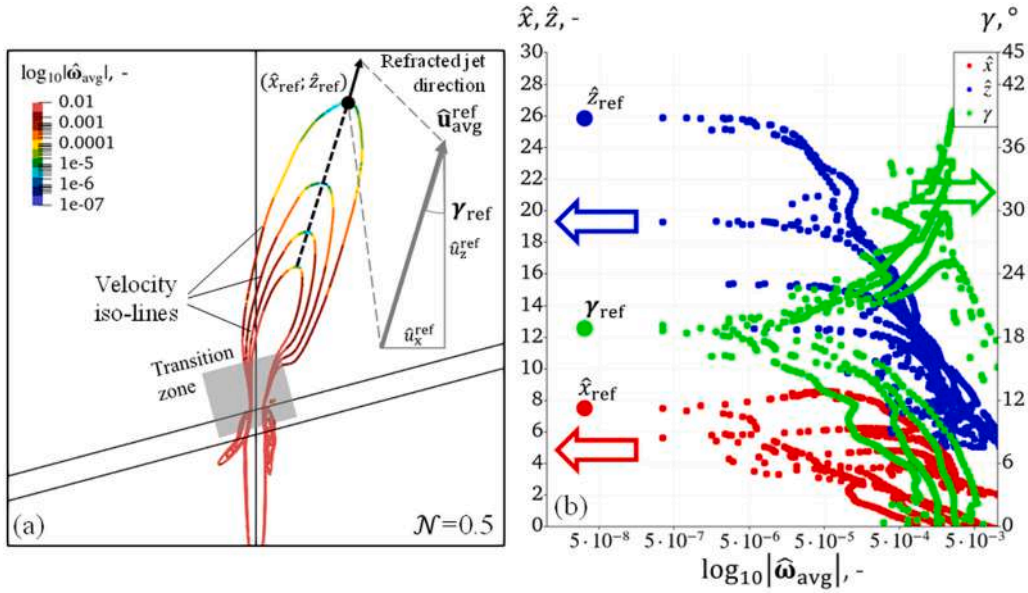


Fig. 18. Calculation schematics of a refracted jet direction (sample data for  $\mathcal{N}=0.5$ ): (a) time-average vorticity  $\widehat{\omega}_{\text{avg}}$  distribution along velocity iso-lines; (b) distribution of the calculated refraction angle  $\gamma$  (in green) at each isoline point with coordinates  $(\widehat{x}; \widehat{z})$  (in red and blue).

$$n_x \cdot \sin \alpha = n_y \cdot \sin \gamma. \tag{16}$$

When applying to the conductive turbulent jet, the first refractive index  $n_x$  is set to 1 for the initial flow regime, which is free from the magnetic field. By setting  $n_x = 1$  in Eq. (16), the final refractive index  $n_y$ , defined for simplicity hereinafter as  $n$ , can be calculated from

$$n = \sin \alpha / \sin \gamma. \tag{17}$$

Using schematics from Fig. 18 together with Eq. (15), the refraction angles  $\gamma$  were recovered for the series of the numerical calculations in Fig. 19(a) for the consequent range of interaction numbers  $\mathcal{N}$  and inclination angles  $\alpha=10^\circ, 15^\circ$  and  $20^\circ$ . The corresponding refractive index  $n$  of a turbulent jet under action of the applied local magnetic field was calculated using Eq. (17) and plotted in Fig. 19 (b). The dashed lines in Fig. 19(b) represent the parabolic trend lines in the reflection zone reflecting similar behavior.

It was observed that for interaction numbers below  $\mathcal{N}=0.5$ , all three curves are nearly identical. This similarity can be attributed to the fact that the jet refraction mechanism and the recirculation flow structure within the magnetic field zone are consistent across different incidence angle values  $\alpha$ , as shown in Fig. 20(a)-(c) for  $\mathcal{N}=0.25$ . Additionally, a key finding was that the refractive index follows a straightforward linear trend for interaction numbers  $\mathcal{N} \leq 0.5$ :

$$n \approx 1 - \mathcal{N}. \tag{18}$$

However, the  $n$  curves start to deviate for higher interaction numbers (e.g.  $\mathcal{N}=0.75$  in Fig. 20(d)-(f) and become completely different as for  $\mathcal{N}=1$  in Fig. 20(g)-(i), where the reverse flow zones are much more pronounced on the jet's right side for the case of higher angle of incidence  $\alpha=20^\circ$

#### 4.2. Influence of the walls (confined jet)

As outlined in the description of the simulated scenarios in Fig. 3, in addition to the case with open boundaries, a scenario involving a wall-confined jet was also modeled. The computational domain is partially open at the top and along the sides parallel to the magnetic field direction. The front and back Hartmann walls, normal to  $\widehat{\mathbf{B}}$ , are electrically conductive, and the bottom Shercliff wall is electrically insulated.

The simulation results for the confined jet are presented in Fig. 21 for a magnetic field inclination angle of  $\alpha=15^\circ$  and interaction numbers  $\mathcal{N}=0.158, 0.75$  and  $1.58$ , as in the previous scenario depicted in Fig. 15 for the free jet. The additional braking effects from the conductive walls are minimal for  $\mathcal{N}=0.158$ , as illustrated in Fig. 21(a)-(c), showing negligible differences compared to Fig. 15(a)-(c), since the induced current loops primarily through the liquid bulk.

However, at a higher magnetic field strength of  $\mathcal{N}=0.75$ , a more pronounced braking effect is observed due to the closure of the induced electric current lines through the conductive side walls. As shown in Fig. 21(d)-(e), the jet is almost entirely reflected, occurring much earlier than in the case of the free jet. Additionally, a secondary flow develops along the vertical walls, as illustrated in Fig. 21(d). At an even higher magnetic field strength of  $\mathcal{N}=1.58$ , the jet becomes fully reflected, leading to the emergence of an

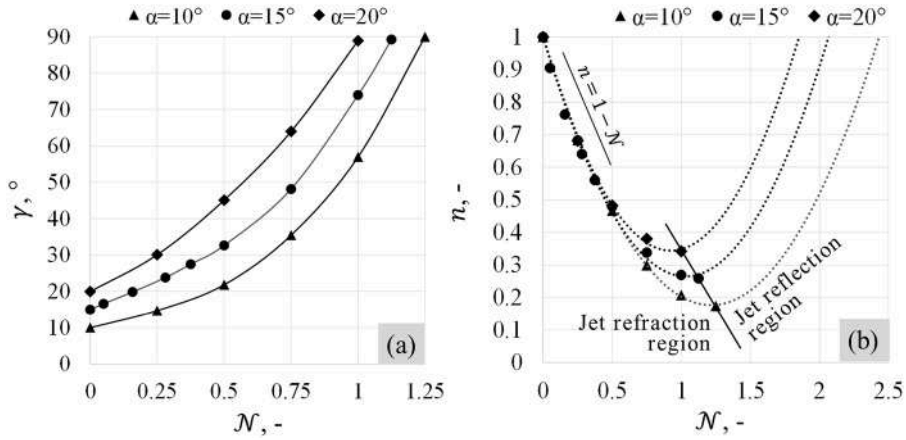


Fig. 19. Distribution of the simulated (a) refraction angle  $\gamma$  and (b) refractive index  $n$  based on the interaction number  $\mathcal{N}$  for the incidence angles of  $\alpha=10^\circ$ ,  $15^\circ$  and  $20^\circ$ .

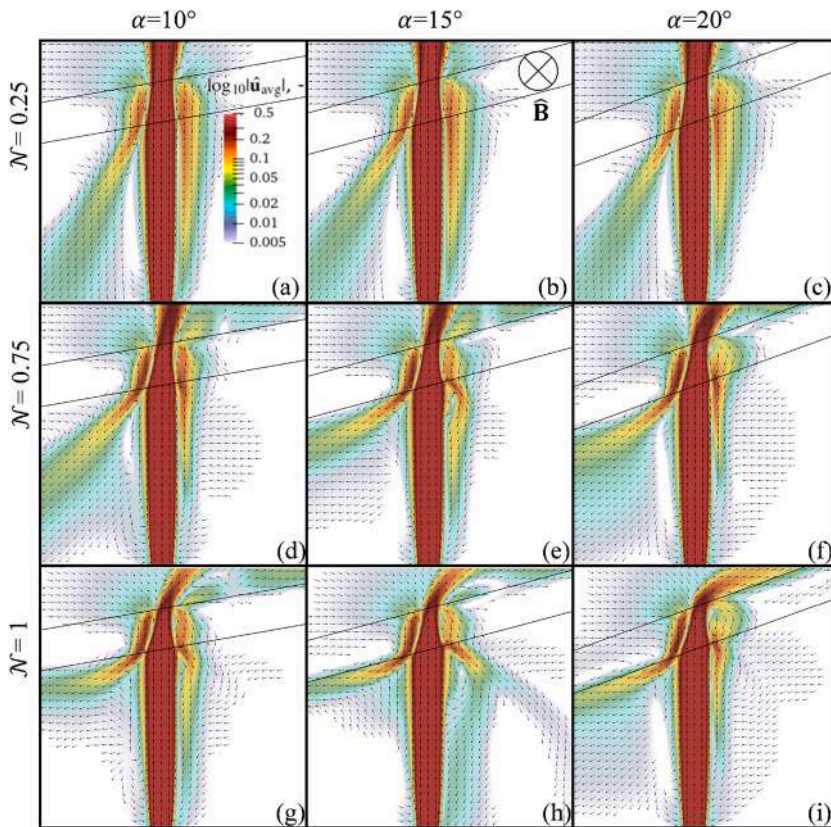
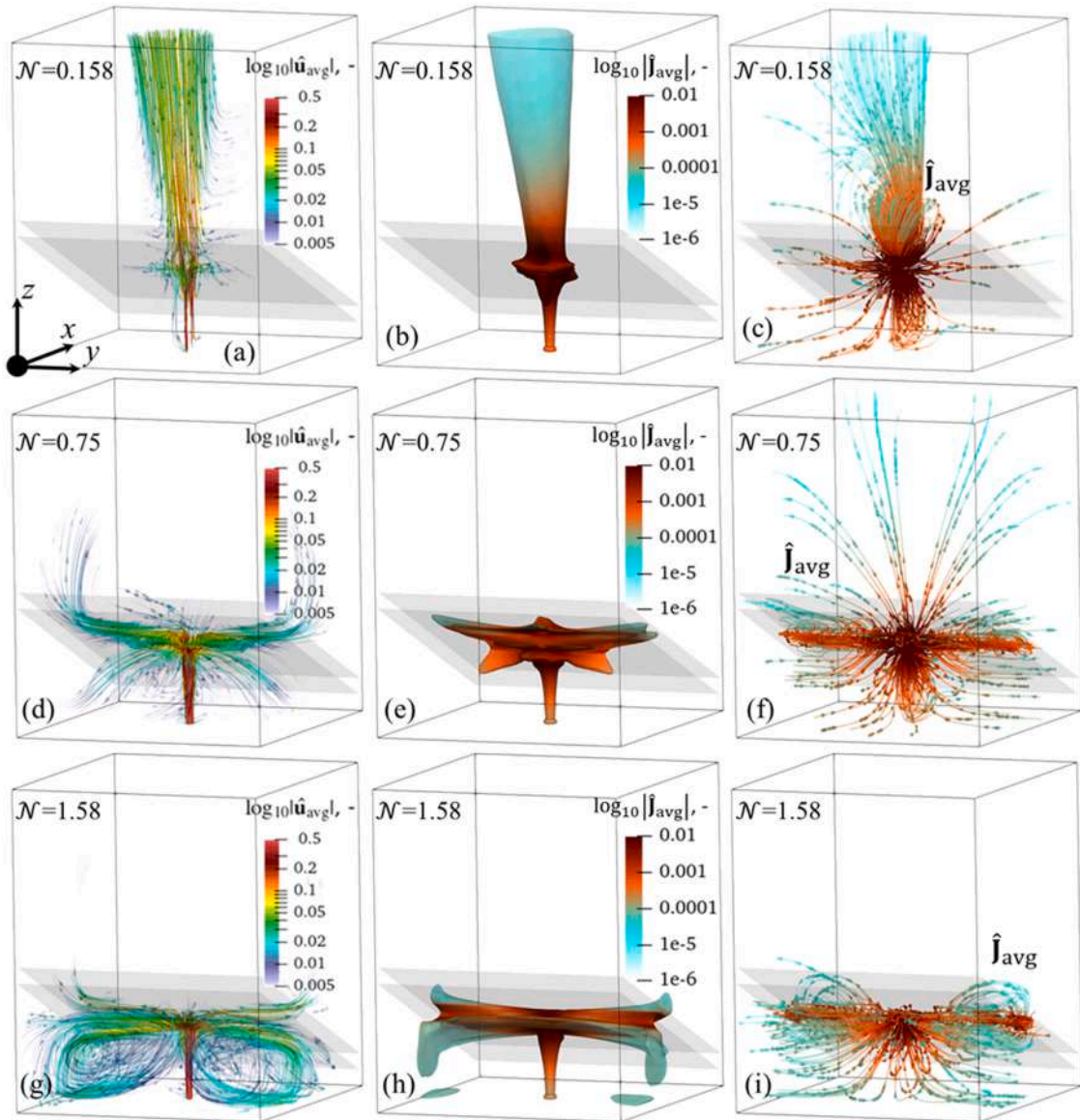


Fig. 20. Structure of the flow zones inside magnetic field zone for different angles of incidence  $\alpha=10^\circ, 15^\circ$  and  $20^\circ$  based on the interaction number  $\mathcal{N}=0.25, 0.75$  and  $1$ .

intriguing "double tube" flow beneath the magnetic field region, as depicted in Fig. 21(g)-(i).

### 4.3. Bending and the widening of the relativistic jets

Fig. 22 presents typical examples of astrophysical jet bending in various systems, such as Cygnus A [45], Centaurus A [46,47], and the radio galaxy 3C31 (NGC 383) [48]. These observations reveal that jets, initially emanating from an active galactic nucleus (AGN), are collimated outflows (see Fig. 22(a)), likely confined by the rotational component of the magnetic field [49]. As depicted in Fig. 22



**Fig. 21.** Confined jet results: time-averaged streamlines (left column), jet shape (isosurface of  $|\hat{\mathbf{u}}_{\text{avg}}| = 0.025$ , middle column) and induced e-current lines (right column) under the inclined by  $\alpha=15^\circ$  magnetic field for the interaction number values (a)–(c)  $\mathcal{N}=0.158$ , (d)–(f)  $\mathcal{N}=0.75$  and (g)–(i)  $\mathcal{N}=1.58$ .

(b), these confined jets bend and widen significantly after traveling a certain distance. The bent jets in Centaurus A offer evidence of relativistic effects, as illustrated in Fig. 22(b). In this figure, the upper tail, oriented towards the observer, exhibits a brighter luminosity than the fading outgoing tail at the bottom. Additionally, the counter-jets exhibit a mirrored bending and spreading pattern (see Fig. 22(c)) relative to both the accretion disk plane and the jet's own axis.

The bending of relativistic jet (RJ) tails is frequently observed, as shown in Fig. 22, though the underlying cause of this bending remains an unresolved issue in astrophysics [50]. Various theoretical and experimental studies address this phenomenon. Fendt and Zinnecker used force balance analysis to propose two potential causes for RJs deflection: (i) the interaction of Lorentz forces between the jet and an inclined interstellar magnetic field, and (ii) the orbital motion of the jet's source within multiple stellar systems [51]. Recent laboratory experiments by Revet et al. [52] investigated the restructuring of outflows in various astrophysical objects, suggesting that misalignment between the ambient magnetic field and the extragalactic jet might explain changes in the jet's direction [52].

Additionally, relativistic jets are thought to be influenced by frame-dragging effects, specifically Lense–Thirring precession, which causes rapid changes in the jet's direction relative to the rotation axis of the accretion disk [53]. This interaction alters the angle between the RJ and the general magnetic field of the AGN system, and the refraction and expansion effects observed in this study could

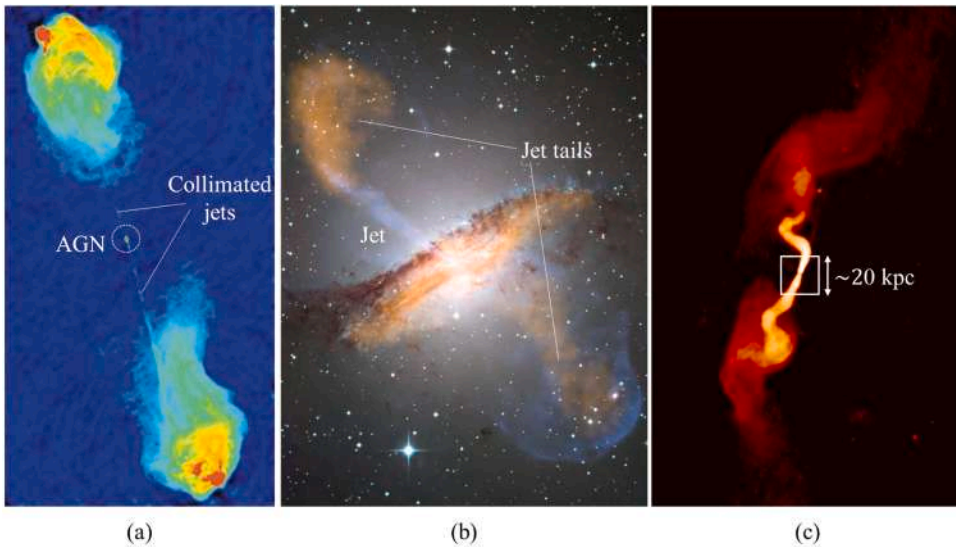


**Fig. 22.** Relativistic jets: (a) Cygnus A [45] (image adapted from the open source Legacy Astronomical Images, “Cygnus A” NRAO / AUI Archives, accessed February 21, 2024, <https://www.nrao.edu/archives/items/show/33385>); (b) Centaurus A [46,47] (image adapted from European Southern Observatory (ESO) image archive licensed under a CCA 4.0, “Centaurus A”, accessed February 21, 2024, <https://www.eso.org/public/images/eso0903a/>); (c) radio galaxy 3C 31 (NGC 383) [48] (image adapted from the open source Legacy Astronomical Images, “Radio Galaxy 3C31” NRAO/AUI Archives, accessed February 21, 2024, <https://www.nrao.edu/archives/items/show/33372>).

impact the corresponding astrophysical jet.

Another crucial concept for understanding the interaction between RJs and magnetic fields is the frozen magnetic flux theory, originally formulated by Hannes Alfvén as the frozen-in flux theorem [54]. This theorem states that for high magnetic Reynolds numbers  $\mathcal{R}_{em}$ , magnetic diffusion is relatively insignificant on the length scale  $L_0$ , and the magnetic field lines are advected with the flow, preserving the magnetic field topology [55]. However, Alfvén later cautioned against relying solely on this theorem, noting that magnetic topology can be altered by diffusion and field line reconnection during complex fluid motion [56]. Modern studies, such as those by Eyink and Aluie [57], have detailed the conditions under which Alfvén’s theorem may break down, showing that in the limit of large  $\mathcal{R}_{em}$ , diffusion and reconnection are minimal, and the magnetic field topology remains preserved [57].

The magnetic Reynolds number can be estimated for the RJs according to Equation (3): the magnetic constant  $\mu_0 = 4\pi \times 10^{-7} \text{ N} \cdot \text{A}^{-2}$  is the vacuum magnetic permeability [58]; the characteristic velocities  $U_0$  range for RJs between 0.1 and 0.5 speeds of light  $c$ , as presented for Cygnus A by Boccardi et al. [59]. Assuming the jet speed within acceleration regions to be at its lowest estimation of  $0.1 c \approx 30 \times 10^6 \text{ m/s}$ , the product  $U_0 \cdot \mu_0$  is of an order of 10. Thus, the  $\mathcal{R}_{em}$  becomes tremendous inside a highly conductive astrophysical jets on a kiloparsec scale [60].

According to Alfvén’s frozen-in flux concept [54], the magnetic field initially advected with a relativistic jet remains attached to it. However, as the jet expands and its velocity decreases significantly, becoming sub-luminous, this coupling with the magnetic field breaks down. While AGN jets are thought to carry helical magnetic fields, their symmetry can be disrupted by surrounding ambient matter and turbulence in the jet’s outer layers [61]. As the jet’s velocity decreases, it begins to interact with the magnetic field at an angle, leading to the observed refraction (bending) effects detected by very long baseline interferometry (VLBI) methods.

Laing and Bridle [48] observed that in the radio galaxy 3C 31, a relativistic jet decelerates from  $0.9 c$  down to  $0.2 c$  over a kiloparsec scale. This transition from the inner to outer region of the jet is highlighted in Fig. 22(c) with a square. Their observations suggest that beyond the outer region, the jets exhibit increasing asymmetries, which Laing and Bridle interpret as evidence of large-scale bending in the 3C 31 system [48].

Integrating these observations with theoretical findings, it is reasonable to conclude that relativistic jets at their outer boundaries interact with strong magnetic fields. This study confirms that a conductive fluid jet expands and refracts upon interacting with a local angled magnetic field. Even when the magnetic field is aligned with the jet axis, the expansion of the jet leads to a reduction in velocity and subsequent instability and fluctuation in the flow.

## 5. Conclusions

In the current study, the interaction of a turbulent jet with a localized transverse magnetic field was examined, focusing on the jet’s inclination angle and the intensity of the magnetic field. The findings reveal that the presence of a direct current (DC) magnetic field induces a phenomenon more complex than mere refraction. Specifically, a transition zone between the point of impact and the final angle causes the jet to adopt a curved “banana” shape, a result that was also experimentally observed by Schurmann et al. [62] in their ultrasonically measured Galinstan SEN jet flow within a continuous casting mold cavity. Beyond the magnetic field area, the refracted

jet expands and exhibits fluctuations in the mean flow.

In addition to the main jet's refraction, the study observed the formation of reversed downward jets on both sides in the plane perpendicular to the magnetic field, as well as two additional reflected jets oriented parallel to the magnetic field lines.

The study explored how the refractive index  $n$  of the main jet depends on the magnetic interaction number  $\mathcal{M}$ . For moderate values of  $\mathcal{M} \leq 0.5$ , a simple relation  $n \approx 1 - \mathcal{M}$  was found, independent of the jet's inclination angle. However, for  $\mathcal{M} > 0.5$ , the refractive index varies significantly with different angles due to the formation of reverse flow zones adjacent to the main jet within the magnetic field.

The presence of conductive walls further enhances the jet's refraction, leading to earlier reflection because of the closure of the induced current density lines through these walls.

The numerical study contributed to developing a theoretical understanding of the bending mechanisms in interstellar relativistic jets. This theory considers: (i) the interaction of relativistic jets with a misaligned ambient magnetic field of active galactic nuclei (AGN), and (ii) the coupled motion of the frozen-in magnetic flux, followed by decoupling and interaction between the magnetic field and the jets as their speed decreases to sub-luminal levels.

### CRedit authorship contribution statement

**Alexander Vakhrushev:** Writing – original draft, Visualization, Software, Methodology, Investigation, Formal analysis. **Ebrahim Karimi-Sibaki:** Writing – review & editing, Validation, Methodology, Investigation, Formal analysis. **Menghuai Wu:** Writing – review & editing, Supervision, Methodology, Formal analysis. **Abdellah Kharicha:** Writing – original draft, Supervision, Project administration, Methodology, Investigation, Formal analysis, Conceptualization.

### Declaration of competing interest

The authors declare that they have no known competing financial interests or personal relationships that could have appeared to influence the work reported in this paper.

### Supplementary materials

Supplementary material associated with this article can be found, in the online version, at [doi:10.1016/j.apm.2025.116124](https://doi.org/10.1016/j.apm.2025.116124).

### Data availability

No data was used for the research described in the article.

### References

- [1] J.H. Beall, A review of astrophysical jets, *APP* 1 (2014) 259–264, <https://doi.org/10.14311/APP.2014.01.0259>.
- [2] M. Livio, Astrophysical jets: a phenomenological examination of acceleration and collimation, *Physics Phys. Rep* 311 (1999) 225–245, [https://doi.org/10.1016/S0370-1573\(98\)00102-1](https://doi.org/10.1016/S0370-1573(98)00102-1).
- [3] K.M. Blundell, M.G. Bowler, Jet velocity in SS 433: its anticorrelation with precession-cone angle and dependence on orbital phase, *ApJ* 622 (2005) L129–L132, <https://doi.org/10.1086/429663>.
- [4] M. Janssen, et al., Event Horizon Telescope observations of the jet launching and collimation in Centaurus A, *Nat. Astron.* 5 (2021) 1017–1028, <https://doi.org/10.1038/s41550-021-01417-w>.
- [5] E. Bañados, et al., An 800-million-solar-mass black hole in a significantly neutral Universe at a redshift of 7.5, *Nature* 553 (2018) 473–476, <https://doi.org/10.1038/nature25180>.
- [6] J. Yang, et al., Pöniuā'ena: a luminous  $z = 7.5$  quasar hosting a 1.5 billion solar mass black hole, *ApJL* 897 (2020) L14, <https://doi.org/10.3847/2041-8213/ab9c26>.
- [7] F. Wang, et al., A luminous quasar at redshift 7.642, *ApJL* 907 (2021) L1, <https://doi.org/10.3847/2041-8213/abd8c6>.
- [8] F. Stefani, Liquid-metal experiments on geophysical and astrophysical phenomena, *Nat. Rev. Phys.* (2024), <https://doi.org/10.1038/s42254-024-00724-1>.
- [9] J. Davelaar, et al., Modeling non-thermal emission from the jet-launching region of M 87 with adaptive mesh refinement, *A&A* 632 (2019) A2, <https://doi.org/10.1051/0004-6361/201936150>.
- [10] A. Mignone, et al., High-resolution 3D relativistic MHD simulations of jets: 3D RMHD simulations of jets, *Mon. Not. R. Astron. Soc.* 402 (2010) 7–12, <https://doi.org/10.1111/j.1365-2966.2009.15642.x>.
- [11] O. Porth, S.S. Komissarov, Causality and stability of cosmic jets, *Mon. Not. R. Astron. Soc.* 452 (2015) 1089–1104, <https://doi.org/10.1093/mnras/stv1295>.
- [12] S. Massaglia, et al., Making Faranoff-Riley I radio sources: I. Numerical hydrodynamic 3D simulations of low-power jets, *A&A* 596 (2016) A12, <https://doi.org/10.1051/0004-6361/201629375>.
- [13] A.Y. Wagner, et al., Galaxy-scale AGN feedback – theory, *Astron. Nachr* 337 (2016) 167–174, <https://doi.org/10.1002/asna.201512287>.
- [14] K.N. Gourgouliatos, S.S. Komissarov, Reconfinement and loss of stability in jets from active galactic nuclei, *Nat. Astron.* 2 (2017) 167–171, <https://doi.org/10.1038/s41550-017-0338-3>.
- [15] S. Massaglia, et al., Making Faranoff-Riley I radio sources: II. The effects of jet magnetization, *A&A* 621 (2019) A132, <https://doi.org/10.1051/0004-6361/201834512>.
- [16] S. Komissarov, O. Porth, Numerical simulations of jets, *New Astron. Rev* 92 (2021) 101610, <https://doi.org/10.1016/j.newar.2021.101610>.
- [17] K. Timmel, S. Eckert, G. Gerbeth, Experimental investigation of the flow in a continuous-casting mold under the influence of a transverse, direct current magnetic field, *Metall. Mater. Trans. B* 42 (2011) 68–80, <https://doi.org/10.1007/s11663-010-9458-1>.

- [18] K. Timmel, et al., Experimental and numerical modeling of fluid flow processes in Continuous casting: results from the LIMMCAST-Project, IOP Conf. Ser. 228 (2017) 012019, <https://doi.org/10.1088/1757-899X/228/1/012019>.
- [19] A. Vakhrushev, et al., Impact of submerged entry nozzle (SEN) immersion depth on meniscus flow in continuous casting mold under electromagnetic brake (EMBr), Metals. (Basel) 13 (2023) 444, <https://doi.org/10.3390/met13030444>.
- [20] E. Mas de, les Valls, Development of a Simulation Tool For MHD Flows Under Nuclear Fusion conditions, Tesi doctoral, Universitat Politècnica de Catalunya, 2011. <http://hdl.handle.net/2117/95157>.
- [21] A. Vakhrushev, et al., Assessment of URANS-type turbulent flow modeling of a single port submerged entry nozzle (SEN) for thin slab continuous casting (TSC) process, Metall. Mater. Trans. B. 55 (2024) 891–904, <https://doi.org/10.1007/s11663-024-03002-8>.
- [22] M. Sedén, B. Rydholm, Numerical simulations of electromagnetic counteractions to mold fluid flow asymmetry deviations, in: IOP Conf. Ser.: Mater. Sci. Eng. 529, 2019 012068, <https://doi.org/10.1088/1757-899X/529/1/012068>.
- [23] A. Vakhrushev, et al., Modeling asymmetric flow in the thin-slab casting mold under electromagnetic brake, Steel. Res. Int. 93 (2022) 2200088, <https://doi.org/10.1002/srin.202200088>.
- [24] A. Vakhrushev, et al., Effects of the asymmetric and oscillating turbulent melt flow on the heat transfer and solidification inside the thin slab continuous casting (TSC) mold under the applied electromagnetic brake (EMBr), J. Phys.: Conf. Ser. 2766 (2024) 012196, <https://doi.org/10.1088/1742-6596/2766/1/012196>.
- [25] A. Kharicha, et al., Reverse flows and flattening of a submerged jet under the action of a transverse magnetic field, Phys. Rev. Fluids. 6 (2021) 123701, <https://doi.org/10.1103/PhysRevFluids.6.123701>.
- [26] A. Vakhrushev, et al., Generation of reverse meniscus flow by applying an electromagnetic brake, Metall. Mater. Trans. B. 52 (2021) 3193–3207, <https://doi.org/10.1007/s11663-021-02247-x>.
- [27] P.A. Davidson, Introduction to Magnetohydrodynamics, 2nd ed., Cambridge University Press, 2016 <https://doi.org/10.1017/9781316672853>.
- [28] I.A. Belyaev, et al., Experimental study of submerged liquid metal jet in a rectangular duct in a transverse magnetic field, J. Fluid. Mech. 953 (2022) A10, <https://doi.org/10.1017/jfm.2022.879>.
- [29] D. Krasnov, et al., Transformation of a submerged flat jet under strong transverse magnetic field, EPL 134 (2021) 24003, <https://doi.org/10.1209/0295-5075/134/24003>.
- [30] A. Vakhrushev, et al., Electric current distribution during electromagnetic braking in continuous casting, Metall. Mater. Trans. B. 51 (2020) 2811–2828, <https://doi.org/10.1007/s11663-020-01952-3>.
- [31] H. Kobayashi, Large eddy simulation of magnetohydrodynamic turbulent channel flows with local subgrid-scale model based on coherent structures, Phys. Fluids 18 (2006) 045107, <https://doi.org/10.1063/1.2194967>.
- [32] V. Todde, P.G. Spazzini, M. Sandberg, Experimental analysis of low-reynolds number free jets: evolution along the jet centerline and reynolds number effects, Exp. Fluids. 47 (2009) 279–294, <https://doi.org/10.1007/s00348-009-0655-0>.
- [33] F. Nicoud, F. Ducros, Subgrid-scale stress modelling based on the square of the velocity gradient tensor, Flow, Turbul. Combust. 62 (1999) 183–200, <https://doi.org/10.1023/A:1009995426001>.
- [34] R. Chaudhary, C. Ji, B.G. Thomas, S.P. Vanka, Transient turbulent flow in a liquid-metal mold of continuous casting, including comparison of six different methods, Metall and Materi Trans B 42 (2011) 987–1007, <https://doi.org/10.1007/s11663-011-9526-1>.
- [35] M.-J. Ni, et al., A current density conservative scheme for incompressible MHD flows at a low magnetic reynolds number. Part II: on an arbitrary collocated mesh, J. Comput. Phys. 227 (2007) 205–228, <https://doi.org/10.1016/j.jcp.2007.07.023>.
- [36] J.H. Ferziger, M. Perić, Computational Methods For Fluid Dynamics, 3rd, rev. ed, Springer, Berlin ; New York, 2002.
- [37] C.M. Rhie, W.L. Chow, Numerical study of the turbulent flow past an airfoil with trailing edge separation, AIAA J 21 (1983) 1525–1532, <https://doi.org/10.2514/3.8284>.
- [38] B. Van Leer, Towards the ultimate conservative difference scheme. V. A second-order sequel to Godunov's method, J. Comput. Phys. 32 (1979) 101–136, [https://doi.org/10.1016/0021-9991\(79\)90145-1](https://doi.org/10.1016/0021-9991(79)90145-1).
- [39] R. Courant, K. Friedrichs, H. Lewy, On the partial difference equations of mathematical physics, IBM J. Res. & Dev. 11 (1967) 215–234, <https://doi.org/10.1147/rd.112.0215>.
- [40] H.G. Weller, G. Tabor, H. Jasak, C. Fureby, A tensorial approach to computational continuum mechanics using object-oriented techniques, Comput. Phys 12 (1998) 620–631, <https://doi.org/10.1063/1.168744>.
- [41] P.A. Davidson, Magnetic damping of jets and vortices, J. Fluid. Mech. 299 (1995) 153–186, <https://doi.org/10.1017/S0022112095003466>.
- [42] J.C.R. Hunt, A.A. Wray, P. Moin, Summer Program 1988, Center for Turbulence Research Report CTR-S88, 1988, pp. 193–208.
- [43] V. Kolář, Vortex identification: new requirements and limitations, Int. J. Heat. Fluid. Flow. 28 (2007) 638–652, <https://doi.org/10.1016/j.ijheatfluidflow.2007.03.004>.
- [44] M. Born, E. Wolf, A.B. Bhatia, Principles of optics: Electromagnetic Theory of propagation, interference, and Diffraction of light, Seventh (expanded) Anniversary edition, 60th Anniversary Edition, Cambridge University Press, Cambridge, 2019.
- [45] R.A. Perley, J.W. Dreher, J.J. Cowan, The jet and filaments in Cygnus A, ApJ 285 (1984) L35, <https://doi.org/10.1086/184360>.
- [46] J.O. Burns, E.D. Feigelson, E.J. Schreier, The inner radio structure of Centaurus A - clues to the origin of the jet X-ray emission, ApJ 273 (1983) 128, <https://doi.org/10.1086/161353>.
- [47] European Southern Observatory (ESO), Centaurus A, 2009. <https://www.eso.org/public/images/eso0903a/>.
- [48] R.A. Laing, A.H. Bridle, Relativistic models and the jet velocity field in the radio galaxy 3C 31, Mon. Not. R. Astron. Soc. 336 (2002) 328–352, <https://doi.org/10.1046/j.1365-8711.2002.05756.x>.
- [49] D.C. Gabuzda, et al., Parsec scale Faraday-rotation structure across the jets of nine active galactic nuclei, Mon. Not. R. Astron. Soc. 472 (2017) 1792–1801, <https://doi.org/10.1093/mnras/stx2127>.
- [50] C.P. O'Dea, S.A. Baum, Wide-angle-tail (WAT) radio sources, Galaxies 11 (2023) 67, <https://doi.org/10.3390/galaxies11030067>.
- [51] C. Fendt, H. Zinnecker, Possible bending mechanisms of protostellar jets, A&A 334 (1998) 750–755.
- [52] G. Revet, et al., Laboratory disruption of scaled astrophysical outflows by a misaligned magnetic field, Nat. Commun. 12 (2021) 762, <https://doi.org/10.1038/s41467-021-20917-x>.
- [53] J.C.A. Miller-Jones, et al., A rapidly changing jet orientation in the stellar-mass black-hole system V404 Cygni, Nature 569 (2019) 374–377, <https://doi.org/10.1038/s41586-019-1152-0>.
- [54] H. Alfvén, Existence of electromagnetic-hydrodynamic waves, Nature 150 (1942) 405–406, <https://doi.org/10.1038/150405d0>.
- [55] P.M. Bellan, Fundamentals of Plasma Physics, Cambridge University Press, Cambridge, 2008.
- [56] H. Alfvén, On frozen-in field lines and field-line reconnection, J. Geophys. Res. 81 (1976) 4019–4021, <https://doi.org/10.1029/JA081i022p04019>.
- [57] G.L. Eyink, H. Aluie, The breakdown of Alfvén's theorem in ideal plasma flows: necessary conditions and physical conjectures, Physica D 223 (2006) 82–92, <https://doi.org/10.1016/j.physd.2006.08.009>.
- [58] W. Baumjohann, R.A. Treumann, Basic Space Plasma Physics, Revised, IMPERIAL COLLEGE PRESS, 2012, <https://doi.org/10.1142/p850>.
- [59] B. Boccardi, et al., The stratified two-sided jet of Cygnus A: acceleration and collimation, A&A 585 (2016) A33, <https://doi.org/10.1051/0004-6361/201526985>.
- [60] B. Boccardi, T.P. Krichbaum, E. Ros, J.A. Zensus, Radio observations of active galactic nuclei with mm-VLBI, Astron. Astrophys. Rev 25 (2017) 4, <https://doi.org/10.1007/s00159-017-0105-6>.
- [61] D.M. Christodoulou, et al., Dominance of outflowing electric currents on decaparsec to kiloparsec scales in extragalactic jets, A&A 591 (2016) A61, <https://doi.org/10.1051/0004-6361/201527448>.
- [62] D. Schurmann, et al., Impact of the electromagnetic brake position on the flow structure in a slab continuous casting mold: an experimental parameter study, Metall. Mater. Trans. B 51 (2020) 61–78, <https://doi.org/10.1007/s11663-019-01721-x>.